Optimal Mach-Zehnder phase sensitivity with Gaussian states

Stefan Ataman [*]

*Extreme Light Infrastructure - Nuclear Physics (ELI-NP), 'Horia Hulubei' National R&D Institute for Physics
and Nuclear Engineering (IFIN-HH), 30 Reactorului Street, 077125 Măgurele, jud. Ilfov, Romania*

We address in this work the phase sensitivity of a Mach-Zehnder interferometer with Gaussian input states. A squeezed-coherent plus squeezed vacuum input state allows us to unambiguously determine the optimal phase-matching conditions in order to maximize the quantum Fisher information. Realistic detection schemes are described and their performance compared with respect to the quantum Cramér-Rao bound. The core of this paper discusses in detail the most general Gaussian input state, without any *a priori* parameter restrictions. Prioritizing the maximization of various terms in the quantum Fisher information has the consequence of imposing the input phase-matching conditions. We discuss in detail when each scenario yields an optimal performance. Realistic detection scenarios are also considered and their performance compared to the theoretical optimum. The impact of the beam splitter types employed on the optimum phase-matching conditions is also discussed. We find a number of potentially interesting advantages of these states over the coherent plus squeezed vacuum input case.

I. INTRODUCTION

Interferometric phase sensitivity is an ongoing research topic benefiting from a high interest from the research community [1–11]. The theoretic works [3–10] are paralleled by the practical interest from the gravitational-wave detection [1,12–15] and quantum technology [6,16] communities.

The shot-noise limited single coherent input interferometer has been long ago shown to be surpassed by the use of nonclassical states of light [2,17–19]. The coherent plus squeezed vacuum input state [20–22] became a popular choice, also due to its good performance in the low- as well as in the high-power regimes [3,7,22]. Recently, the squeezing technique has been shown to reduce laser power fluctuations [15], detect mechanical motion of an oscillator [23], or help the search for axionlike particles [24]. For a recent review on the applications of squeezed states, see Ref. [25].

After the first round of observations, the gravitational-wave observatories enhanced their sensitivities by employing squeezed states of light [26]. Boosted by these needs, the generation of squeezed light became a mature technology [27,28] delivering ever increasing squeezing factors [14].

The phase sensitivity of a Mach-Zehnder interferometer (MZI) is generally not constant over a wide range of total internal phase shifts [7,11,29] and it depends on the detection scheme employed [3,10,11,22]. Although for some states, workarounds to extend this range are known [30], it is generally preferred to operate the interferometer at or near the optimum working point φ_{opt} (sometimes also called the "sweet spot"). For a difference-intensity detection scheme the optimum working point is generally at $\varphi_{\mathrm{opt}} = \pi/2$. This is true for a wide class of input states including the single

coherent, coherent plus squeezed vacuum, as well as the squeezed-coherent plus squeezed vacuum states [6,7,9,31]. In Refs. [7,9] it has been shown that generally $\varphi_{\mathrm{opt}} \neq \pi/2$ for a double coherent input. In this paper we will show that this is also the case for the most general input Gaussian state, namely the squeezed-coherent plus squeezed-coherent input. Other realistic detection schemes yield other optimum internal phase shifts. For example a single-mode intensity and the homodyne detection schemes have the optimum working point $\varphi_{\mathrm{opt}} \approx \pi$ for a large class of input states [3,7].

The quantum Fisher information (QFI) and its associated quantum Cramér-Rao bound (QCRB) [11,32–34] has been shown to be a powerful tool in setting upper performance bounds in phase estimation. We will employ a two-parameter Fisher information calculation [5,21,34] in order to avoid accounting fictitious resources that are actually unavailable [8,11,21].

The QFI approach was applied to single coherent, dual coherent, and coherent plus squeezed vacuum input scenarios [5,7,20,21], thus providing ways to evaluate the suboptimality of realistic detection schemes [3,7]. The most general squeezed-coherent plus squeezed-coherent input was considered in the literature [35,36] with a single-parameter Fisher estimation technique. This approach yielded overoptimistic results by counting resources that are actually not available. The origin of this type of discrepancy was discussed by Jarzyna *et al.* [21]. Moreover, the coherent sources as well as one squeezing operator were assumed to have zero phase [35,36]. In this paper we reconsider this input state, however we insist on not *a priori* limiting any input parameter.

The effect of input phase matching (i.e., the relative phases of the various input sources) has been discussed in the literature [9,21,37]. In [9], this problem was thoroughly analyzed for an unbalanced interferometer. Generally assumed phase-matching conditions set all input phases to zero [21,31,37].

_____
[*]stefan.ataman@eli-np.ro

As shown in Ref. [9], this is not always the optimal choice. In this paper the input phase-matching conditions (PMCs) will be a central point in the discussion. They will prove to be of paramount importance in the characterization of the squeezed-coherent plus squeezed-coherent input scenario. As we will show, the three phase-matching conditions that appear will be consequences of the maximization of the Fisher information and not *a priori* assumptions.

Losses adversely affect the phase sensitivity and we can distinguish between internal losses (photon absorption, decoherence, etc.) [38–40] and the nonideality of the photodetectors [36,41]. In this work we only consider the latter and evaluate their impact on the interferometric phase sensitivity performance.

An often ignored problem is also considered in this paper, namely the impact of the types beam splitters used on the optimum PMCs. Indeed, two main types of beam splitters are used today and this also divides the works in this field: the ones employing symmetrical beam splitters [5–7,9,37] and the ones employing cube beam splitters [3,31,35,36]. As we will show, this choice is not without consequences on the optimum PMCs, sometimes giving the impression that different papers give different accounts for the same input state.

This paper is structured as follows. In Sec. II we formalize our tools used throughout this paper. Among them we introduce two functions, we specify the field operator transformations for our interferometer, and define the Cramér-Rao bound as well as the realistic detection schemes considered. The squeezed-coherent plus squeezed vacuum input with all its consequences is considered in Sec. III. The most general case involving Gaussian states, i.e., the squeezed-coherent plus squeezed-coherent input is thoroughly analyzed in Sec. IV. The impact of the types of beam splitter used on the optimum input phase-matching conditions is discussed in Sec. V. Finally, conclusions are drawn in Sec. VI.

II. MZI SETUP: DETECTION SENSITIVITIES

A. Parameter estimation: A short introduction

We briefly review the problem of parameter estimation in quantum mechanics. Longer introductions are available in the literature [7,11,34,42].

We assume an experimentally accessible Hermitian operator $\hat{A}$ that depends on a parameter φ. In our case this parameter is the internal phase shift in a Mach-Zehnder interferometer. The fact that φ may or may not be an observable makes no difference in our case since we estimate it through the observable $\hat{A}$. The average of this operator is $\langle \hat{A}(\varphi) \rangle = \langle \psi | \hat{A}(\varphi) | \psi \rangle$ where $|\psi\rangle$ is the wave function of the system. The *sensitivity* $\Delta\varphi$ is defined by [7,9,11,42]

$$\Delta\varphi = \frac{\Delta\hat{A}}{\left| \frac{\partial}{\partial\varphi} \langle \hat{A} \rangle \right|}, \quad (1)$$

where the standard deviation is defined as $\Delta\hat{A} = \sqrt{\Delta^2\hat{A}}$ and the variance is $\Delta^2\hat{A} = \langle \psi | \hat{A}^2 | \psi \rangle - \langle \hat{A} \rangle^2$.

Throughout this paper, the explicit dependence on φ of various averages and variances is not necessarily emphasized, i.e., for simplicity we write $\langle \hat{N} \rangle$ instead of $\langle \hat{N}(\varphi) \rangle$, etc.
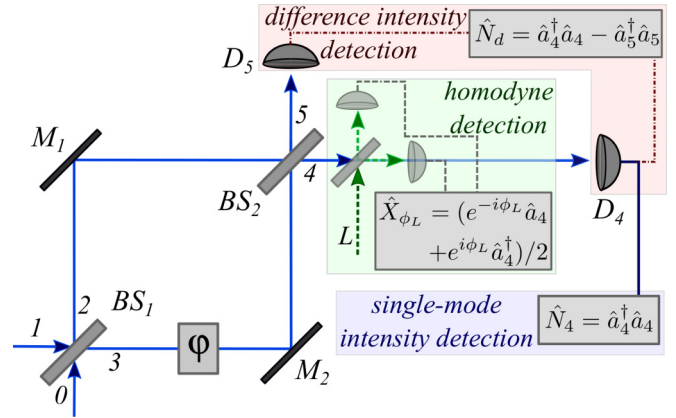

FIG. 1. The detection schemes and their observables for the MZI we analyze here. The parameter to be estimated via a suitable observable is the phase difference φ between the two arms of the MZI.

B. Transformations of the field operators

We consider a balanced Mach-Zehnder interferometer (see Fig. 1). It is composed of two symmetrical beam splitters (BS). We have the well-known field operator transformations, e.g., for the first BS we have [29,43]

$$\hat{a}_0^\dagger = \frac{1}{\sqrt{2}}\hat{a}_2^\dagger + \frac{i}{\sqrt{2}}\hat{a}_3^\dagger,$$
$$\hat{a}_1^\dagger = \frac{i}{\sqrt{2}}\hat{a}_2^\dagger + \frac{1}{\sqrt{2}}\hat{a}_3^\dagger, \quad (2)$$

where $\hat{a}_k$ ($\hat{a}_k^\dagger$) denotes the annihilation (creation) operator on port k. The two input (output) ports are denoted by 0 and 1 (4 and 5). The input-output field operator transformations for the MZI are given by

$$\hat{a}_4^\dagger = -\sin\left(\frac{\varphi}{2}\right)\hat{a}_0^\dagger + \cos\left(\frac{\varphi}{2}\right)\hat{a}_1^\dagger,$$
$$\hat{a}_5^\dagger = \cos\left(\frac{\varphi}{2}\right)\hat{a}_0^\dagger + \sin\left(\frac{\varphi}{2}\right)\hat{a}_1^\dagger, \quad (3)$$

and we ignored global phases. Unless otherwise specified, we assume that the output ports 4 and 5 are connected to ideal photodetectors. No losses inside the MZI are considered throughout this paper.

In the following we denote by φ the total phase shift inside the interferometer. It is composed of two parts: (i) the experimentally controllable part φ_{expt} and (ii) the unknown phase shift φ_s, which is the quantity we want to measure. We have

$$\varphi = \varphi_s + \varphi_{\mathrm{expt}}. \quad (4)$$

In all realistic detection scenarios an *optimum total internal phase shift* φ_{opt} (sometimes called "working point" or "sweet spot") exists. It is desirable to have φ as close as possible to φ_{opt}. If $|\varphi_s| \ll |\varphi|$, this is generally possible by adjusting the experimentally available parameter φ_{expt}.

When speaking of a phase sensitivity at any given total internal phase shift (4) we will denote it with $\Delta\varphi$ and it it is generally a function of φ. When speaking about the phase sensitivity *at* the optimum working point (i.e., when the total internal phase shift is φ_{opt}), we will denote it by $\Delta\tilde{\varphi}$.

C. Output observables

We consider three realistic detection schemes, each one having an associated observable.

In the difference intensity detection scheme we calculate the difference between the output photocurrents (i.e., at the detectors D_4 and D_5, see Fig. 1). This is a very popular setup, especially at low intensities [30]. Thus, the observable conveying information about the phase φ is

$$\hat{N}_d(\varphi) = \hat{n}_4 - \hat{n}_5, \tag{5}$$

where $\hat{n}_k = \hat{a}_k^\dagger \hat{a}_k$ is the number operator for mode k. Using the field operator transformations equations (3) we have

$$\langle \hat{N}_d \rangle = \cos\varphi(\langle \hat{n}_1 \rangle - \langle \hat{n}_0 \rangle) - 2\sin\varphi \mathrm{Re}\langle \hat{a}_0 \hat{a}_1^\dagger \rangle, \tag{6}$$

where the expectation values are calculated with respect to (w.r.t.) the input state $|\psi_{in}\rangle$ and Re denotes the real part. To estimate the phase sensitivity in Eq. (1) we need the absolute value of the derivative

$$\left| \frac{\partial \langle \hat{N}_d \rangle}{\partial \varphi} \right| = |\sin\varphi(\langle \hat{n}_0 \rangle - \langle \hat{n}_1 \rangle) - 2\cos\varphi \mathrm{Re}\langle \hat{a}_0 \hat{a}_1^\dagger \rangle|. \tag{7}$$

The calculation of the standard deviation $\Delta\hat{N}_d$ needed in Eq. (1) is detailed in Appendix B 1.

In the single-mode intensity detection scheme we have only one detector coupled at the output port 4, see Fig. 1. Thus the operator of interest is $\hat{N}_4 = \hat{a}_4^\dagger \hat{a}_4$. From Eq. (3) we have

$$\langle \hat{N}_4 \rangle = \sin^2\left(\frac{\varphi}{2}\right)\langle \hat{n}_0 \rangle + \cos^2\left(\frac{\varphi}{2}\right)\langle \hat{n}_1 \rangle - \sin\varphi \mathrm{Re}\langle \hat{a}_0 \hat{a}_1^\dagger \rangle \tag{8}$$

and the absolute value of its derivative w.r.t. φ is

$$\left| \frac{\partial \langle \hat{N}_4 \rangle}{\partial \varphi} \right| = \frac{1}{2}|\sin\varphi(\langle \hat{n}_0 \rangle - \langle \hat{n}_1 \rangle) - 2\cos\varphi \mathrm{Re}\langle \hat{a}_0 \hat{a}_1^\dagger \rangle|. \tag{9}$$

Similar to the difference-intensity detection scheme, the calculation of the standard deviation $\Delta\hat{N}_4$ is detailed in Appendix B 2.

If we assume a (balanced) homodyne detection at the output port 4, the operator modeling this detection scheme is given by $\hat{X}_{\phi_L} = (e^{-i\phi_L}\hat{a}_4 + e^{i\phi_L}\hat{a}_4^\dagger)/2$ and, expressed with respect to the input field operators,

$$\hat{X}_{\phi_L} = -\sin\left(\frac{\varphi}{2}\right)\frac{e^{-i\phi_L}\hat{a}_0 + e^{i\phi_L}\hat{a}_0^\dagger}{2}$$
$$+ \cos\left(\frac{\varphi}{2}\right)\frac{e^{-i\phi_L}\hat{a}_1 + e^{i\phi_L}\hat{a}_1^\dagger}{2}, \tag{10}$$

where ϕ_L is the phase of the local coherent source (assumed fixed and adjustable with respect to θ_α).

D. Fisher information and the Cramér-Rao bound

The Fisher information is a powerful approach to find the best-case solution of parameter estimation [5,11,32,34,42]. The lower bound for the estimation of a parameter φ is given by the Cramér-Rao bound (CRB) [11,42]. The Fisher information is maximized by the QFI $\mathcal{F}(\varphi)$ [11,32] and this leads to the QCRB,

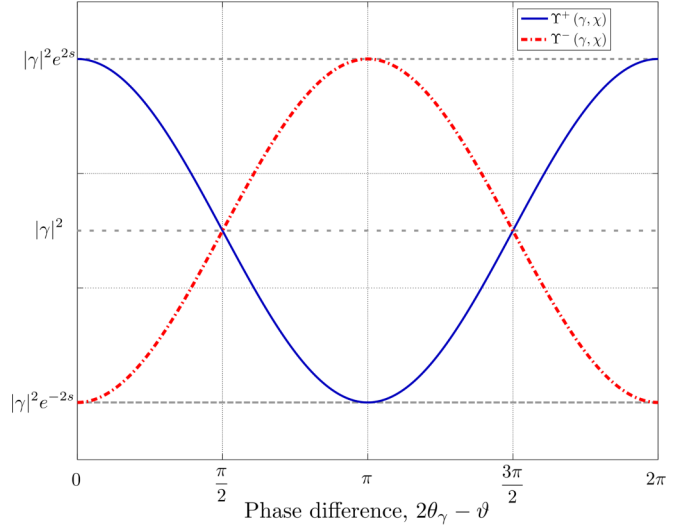$$\Delta\varphi_{\mathrm{QCRB}} = \frac{1}{\sqrt{\mathcal{F}}}. \tag{11}$$

FIG. 2. The functions $\Upsilon^+(\gamma, \chi)$ and $\Upsilon^-(\gamma, \chi)$. For the input phase-matching condition $2\theta_\gamma - \vartheta = 0$ we have $\Upsilon^+(\gamma, \chi) = |\gamma|^2 e^{2s}$ and $\Upsilon^-(\gamma, \chi) = |\gamma|^2 e^{-2s}$.

Since we will be interested in the difference phase shift sensitivity only (see details in Appendix A), we define the QFI as

$$\mathcal{F} = \mathcal{F}_{dd} - \frac{(\mathcal{F}_{sd})^2}{\mathcal{F}_{ss}}. \tag{12}$$

Similar to Ref. [9], we will not consider $\mathcal{F} \approx \mathcal{F}_{dd}$, as done by many authors [5,6]. Although some input states justify this approximation (for example the coherent plus squeezed vacuum input), in our case the Fisher matrix coefficient $\mathcal{F}_{sd}$ from Eq. (A7) will play an important role in the discussion from Sec. IV.

For N repeated experiments we have a scaling $\Delta\varphi_{\mathrm{QCRB}} = 1/\sqrt{N\mathcal{F}}$ [11,32] and the same $1/\sqrt{N}$ applies to $\Delta\varphi$ from Eq. (1). For simplicity, we consider $N = 1$ throughout our discussion.

E. Two useful functions

We now introduce two functions that will repeatedly appear in our calculations, allowing a more compact writing of the obtained results. We define the function

$$\Upsilon^+(\gamma, \chi) = |\gamma|^2[\cosh 2s + \sinh 2s \cos(2\theta_\gamma - \vartheta)], \tag{13}$$

where both arguments are complex and we have $\gamma = |\gamma|e^{i\theta_\gamma}$ and $\chi = se^{i\vartheta}$ with $s \in \mathbb{R}^+$, $\theta_\gamma, \vartheta \in [0, 2\pi]$. Similarly, we introduce the function

$$\Upsilon^-(\gamma, \chi) = |\gamma|^2[\cosh 2s - \sinh 2s \cos(2\theta_\gamma - \vartheta)]. \tag{14}$$

We plot these functions in Fig. 2. In our context, these functions will model the squeezing-induced (χ) enhancement or reduction of the coherent source's (γ) fluctuations. Indeed, one can see that if we impose the phase-matching condition (PMC) $2\theta_\gamma - \vartheta = 0$ ($2\theta_\gamma - \vartheta = \pi$), we have $\Upsilon^+(\gamma, \chi) = |\gamma|^2 e^{2s}$ [$\Upsilon^+(\gamma, \chi) = |\gamma|^2 e^{-2s}$] and $\Upsilon^-(\gamma, \chi) = |\gamma|^2 e^{-2s}$ [$\Upsilon^-(\gamma, \chi) = |\gamma|^2 e^{2s}$], i.e., the fluctuations are enhanced or reduced.

We can also connect these functions to the quadrature measurement at a given angle $\hat{X}_{\theta_q}$ (Ref. [43], Eq. (7.7), Sec. 7.1). Thus, the function $\Upsilon^+(\gamma, \chi)$ is proportional to the fluctuations of quadrature measurement on the $\theta_L = 2\theta_\gamma - \vartheta$ axis while $\Upsilon^-(\gamma, \chi)$ is proportional to the measurement on the $\theta_L = 2\theta_\gamma - \vartheta + \pi/2$ axis. More precisely, we have

$$\Upsilon^+(\gamma, \chi) = 4|\gamma|^2 \Delta^2 \hat{X}_{2\theta_\gamma - \vartheta},$$
$$\Upsilon^-(\gamma, \chi) = 4|\gamma|^2 \Delta^2 \hat{X}_{2\theta_\gamma - \vartheta + \frac{\pi}{2}}. \quad (15)$$

For $\theta_L = 0$ ($\theta_L = \pi/2$) we have a measurement on the X_1 (X_2) quadrature (sometimes called X and Y, e.g., [44], Eqs. (5.6.7) and (5.6.8), Sec. 5.6).

III. SQUEEZED-COHERENT PLUS SQUEEZED VACUUM INPUT

In the first scenario we consider a squeezed-coherent plus squeezed vacuum [9] input state,

$$|\psi_{\text{in}}\rangle = |(\alpha\zeta)_1 \xi_0\rangle = \hat{D}_1(\alpha)\hat{S}_1(\zeta)\hat{S}_0(\xi)|0\rangle \quad (16)$$

applied to the input of the interferometer. A squeezed vacuum state is obtained by applying the squeezing operator [43,45]

$$\hat{S}_m(\chi) = e^{[\chi^* \hat{a}_m^2 - \chi(\hat{a}_m^\dagger)^2]/2}, \quad (17)$$

with $\chi = se^{i\vartheta}$ to a port m previously found in the vacuum state $|0\rangle$. We call $s \in \mathbb{R}^+$ the squeezing factor and ϑ is the phase of the squeezed state. For the input state (16) we use a squeezed state with $\xi = re^{i\theta}$ ($\zeta = ze^{i\phi}$) applied to the input port 0 (1). The displacement operator [43,46,47] for a port k is defined by

$$\hat{D}_k(\alpha) = e^{\alpha \hat{a}_k^\dagger - \alpha^* \hat{a}_k}. \quad (18)$$

Please note that in the input state from Eq. (16) we first *squeeze* and then *displace* the vacuum from input port 1.

We also note that our state is separable (nonentangled), i.e., we can write Eq. (16) as $|\psi_{\text{in}}\rangle = |(\alpha\zeta)_1\rangle \otimes |\xi_0\rangle$. The same remark will apply to the input state discussed in Sec. IV. First, this state of facts corresponds to the experimental reality. Second, by forbidding entanglement at the input of our interferometer, we avoid pathologies connected to the Fisher information (see, e.g., [6] and references within).

A. Fisher information and the Cramér-Rao bound

Our input state (16) applied to Eq. (A6) yields the difference-difference Fisher matrix element [9]

$$\mathcal{F}_{dd} = \Upsilon^+(\alpha, \xi) + \frac{\cosh 2r \cosh 2z}{2} - \frac{\sinh 2r \sinh 2z \cos(\theta - \phi) + 1}{2}. \quad (19)$$

Since $\mathcal{F}_{sd} = 0$ for this input state, we have $\mathcal{F} = \mathcal{F}_{dd}$. The function $\Upsilon^+(\alpha, \xi)$ reaches its maximum value of $|\alpha|^2 e^{2r}$ if we impose the input PMC

$$2\theta_\alpha - \theta = 0 \quad (20)$$

and this is the same constraint already reported and discussed in the literature for the coherent plus squeezed vacuum input [7,20,37]. In order to maximize the last term from Eq. (19)

we have to impose the supplementary input phase-matching condition

$$\theta - \phi = \pm\pi, \quad (21)$$

yielding the optimum QFI

$$\mathcal{F} = |\alpha|^2 e^{2r} + \sinh^2(r + z) \quad (22)$$

and thus the QCRB for the input state (16),

$$\Delta\varphi_{\text{QCRB}} = \frac{1}{\sqrt{|\alpha|^2 e^{2r} + \sinh^2(r + z)}}. \quad (23)$$

B. Difference intensity detection scheme

The input state (16) applied to Eq. (6) gives

$$\langle\hat{N}_d\rangle = \cos\varphi(|\alpha|^2 + \sinh^2 z - \sinh^2 r). \quad (24)$$

For the variance (see details in Appendix D 2) we obtain

$$\Delta^2 \hat{N}_d = \cos^2 \varphi \left(\frac{\sinh^2 2r}{2} + \frac{\sinh^2 2z}{2} + \Upsilon^-(\alpha, \zeta) \right)$$
$$+ \sin^2 \varphi \left(\Upsilon^-(\alpha, \xi) \right.$$
$$\left. + \frac{\cosh 2r \cosh 2z + \sinh 2r \sinh 2z \cos(\phi - \theta) - 1}{2} \right) \quad (25)$$

and the phase sensitivity is given by Eq. (D6). The best sensitivity is achieved for the optimum total internal phase shift $\varphi_{\text{opt}} = \pi/2$. Introducing this result in Eq. (D6) takes us to the best achievable phase sensitivity

$$\Delta\tilde{\varphi}_{\text{df}} = \frac{\sqrt{\Upsilon^-(\alpha, \xi) + \frac{\cosh 2r \cosh 2z + \sinh 2r \sinh 2z \cos(\phi - \theta) - 1}{2}}}{||\alpha|^2 + \sinh^2 z - \sinh^2 r|}. \quad (26)$$

The phase sensitivity is further improved by imposing the phase-matching conditions (20) and (21) yielding

$$\Delta\tilde{\varphi}_{\text{df}} = \frac{\sqrt{|\alpha|^2 e^{-2r} + \sinh^2(r - z)}}{||\alpha|^2 + \sinh^2 z - \sinh^2 r|}. \quad (27)$$

C. Single-mode intensity detection scheme

For the input state (16) the average number of photons for a single-intensity detection scheme is

$$\langle\hat{N}_4\rangle = \sin^2\left(\frac{\varphi}{2}\right) \sinh^2 r + \cos^2\left(\frac{\varphi}{2}\right)(|\alpha|^2 + \sinh^2 z). \quad (28)$$

The variance is found to be (see details in Appendix D)

$$\Delta^2 \hat{N}_4 = \cos^4\left(\frac{\varphi}{2}\right) \left(\frac{\sinh^2 2z}{2} + \Upsilon^-(\alpha, \zeta) \right)$$
$$+ \sin^4\left(\frac{\varphi}{2}\right) \frac{\sinh^2 2r}{2} + \frac{\sin^2 \varphi}{4} \left(\Upsilon^-(\alpha, \xi) \right.$$
$$\left. + \frac{\cosh 2r \cosh 2z + \sinh 2r \sinh 2z \cos(\theta - \phi) - 1}{2} \right) \quad (29)$$

and the phase sensitivity $\Delta\varphi_{\text{sg}}$ in the single-intensity detection scenario is given by Eq. (D7). We can find an optimum internal phase shift,

$$\varphi_{\text{opt}} = \pm 2 \arctan \sqrt[4]{\frac{\sinh^2 2z + 2\Upsilon^-(\alpha,\zeta)}{\sinh^2 2r}} \qquad (30)$$

and introducing this result into Eq. (D7) yields the best achievable phase sensitivity $\Delta\tilde{\varphi}_{\text{sg}}$ from Eq. (D8). This sensitivity can be further improved by imposing the input phase-matching conditions (20) and (21) yielding the result from Eq. (D9).

D. Homodyne detection scheme

Using the results from Appendix B 3 we find

$$|\partial_\varphi \langle \hat{X}_{\phi_L} \rangle| = \frac{1}{2} \left| \sin\left(\frac{\varphi}{2}\right) |\alpha| \cos(\phi_L - \theta_\alpha) \right|. \qquad (31)$$

We impose $\cos(\phi_L - \theta_\alpha) = 1$ thus $\phi_L = \theta_\alpha$, i.e., the local oscillator should be in phase with the coherent source. We find the variance

$$\Delta^2 \hat{X}_{\phi_L} = \frac{\cos^2\left(\frac{\varphi}{2}\right)\Upsilon^-(\alpha,\zeta) + \sin^2\left(\frac{\varphi}{2}\right)\Upsilon^-(\alpha,\xi)}{4|\alpha|^2}, \qquad (32)$$

thus yielding a phase sensitivity

$$\Delta\varphi_{\text{hom}} = \frac{\sqrt{\Upsilon^-(\alpha,\xi) + \cot^2\left(\frac{\varphi}{2}\right)\Upsilon^-(\alpha,\zeta)}}{|\alpha|^2}. \qquad (33)$$

At the optimum angle $\varphi_{\text{opt}} = \pi$ the sensitivity becomes

$$\Delta\tilde{\varphi}_{\text{hom}} = \frac{\sqrt{\Upsilon^-(\alpha,\xi)}}{|\alpha|^2} \qquad (34)$$

and further imposing the PMC (20) yields $\Delta\tilde{\varphi}_{\text{hom}} = e^{-r}/|\alpha|$, a result identical to the one with a coherent plus squeezed vacuum input [3].

E. Discussion

1. Analysis of the obtained results

Using the PMCs given by Eqs. (20) and (21), if we compare the best achievable sensitivities at the optimal working point, we actually have

$$\Delta\tilde{\varphi}_{\text{sg}} \geqslant \Delta\tilde{\varphi}_{\text{df}} \geqslant \Delta\varphi_{\text{QCRB}} \quad \text{and} \quad \Delta\tilde{\varphi}_{\text{hom}} \geqslant \Delta\varphi_{\text{QCRB}} \qquad (35)$$

showing that all discussed schemes are suboptimal. We note that in the case with equal squeezing in both inputs ($r = z$) we find the interesting result

$$\Delta\tilde{\varphi}_{\text{hom}} = \Delta\tilde{\varphi}_{\text{df}} = \frac{e^{-r}}{|\alpha|}. \qquad (36)$$

In the high-$|\alpha|$ regime (i.e., when $|\alpha|^2 \gg \{\sinh^2 r, \sinh^2 z\}$) we have $\Delta\tilde{\varphi}_{\text{sg}} \approx \Delta\tilde{\varphi}_{\text{df}} \approx \Delta\tilde{\varphi}_{\text{hom}} \approx \Delta\varphi_{\text{QCRB}} \approx e^{-r}/|\alpha|$.

In Fig. 3 we plot the realistic detection schemes against the QCRB in the low-$|\alpha|$ limit for two scenarios: $z = 0$ (i.e., no squeezing in port 1) and $z = 2.2$. One notes the swift enhancement in sensitivity in the case of a difference intensity detection scheme (solid red and dashed orange curves), due to the supplementary squeezing. For the single-mode intensity detection scheme (dashed blue and dash-dotted cyan curves),
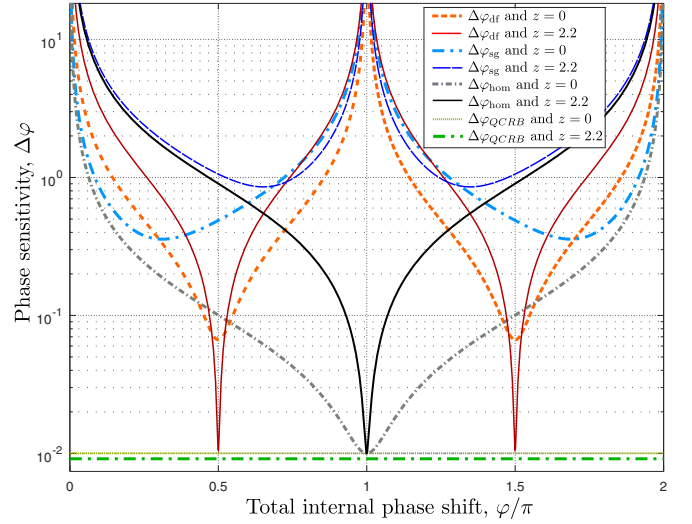

FIG. 3. The phase sensitivity $\Delta\varphi$ versus the phase shift in the low-$|\alpha|$ regime. Adding squeezing does not noticeably enhance the quantum Cramér-Rao bound, however it substantially enhances the performance of a difference-intensity detection scheme. Parameters used: $|\alpha| = 10$, $r = 2.3$, $\theta = 0$, $\theta_\alpha = 0$, and $\phi = \pi$.

on the contrary: the supplementary squeezing simply degrades the performance with respect to no squeezing in port 1.

The best sensitivity reached by a homodyne detection, with or without squeezing in port 1 (dash-dotted gray and solid black curves), reaches the same value: $\Delta\tilde{\varphi}_{\text{hom}} = e^{-r}/|\alpha|$. In this case, too, the second squeezing (ζ) brings no benefit, quite on the contrary: without squeezing in port 1 the sensitivity degrades slower when $\varphi \neq \pi/2$. From Eq. (33) we immediately find the culprit: the $\Upsilon^-(\alpha,\zeta)$ term. Indeed, employing the PMC from Eq. (21) maximized this term to $|\alpha|^2 e^{2z}$. We return shortly to this problem.

From Fig. 3 it is apparent that the gain we found for the difference intensity detection scenario is rather fragile. Indeed, if the internal phase shift drifts from $\varphi_{\text{opt}} = (2k+1)\pi/2$ (with $k \in \mathbb{Z}$), the performance quickly degrades. Tracing back this issue in $\Delta^2 \hat{N}_d$ from Eq. (25), one notes that for the phase-matching conditions given by Eqs. (20) and (21) we have $\Upsilon^-(\alpha,\xi)$ minimized to $|\alpha|^2 e^{-2r}$, however $\Upsilon^-(\alpha,\zeta)$ is maximized again to $|\alpha|^2 e^{2z}$. Thus, as soon as $\cos\varphi \neq 0$, the contribution of $\Upsilon^-(\alpha,\zeta)$ is far from negligible, hence the swift degradation in phase sensitivity. We might conclude at this point that, with the exception of the difference-intensity detection scheme, adding a second squeezing actually worsens the overall performance.

Nonetheless, if we relax our restrictions on the phase-matching conditions leading to the optimal QFI from Eq. (22), many useful advantages will arise from adding a second squeezing. We thus alter now the second phase-matching condition given by Eq. (21) to

$$\theta - \phi = 0. \qquad (37)$$

This new PMC, when replacing the optimal $\theta - \phi = \pm\pi$ constraint, decreases the QFI from the value given in Eq. (22) to

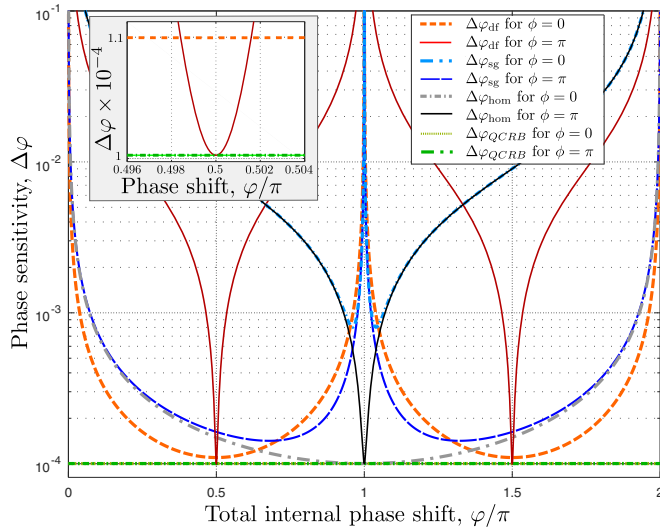$$\mathcal{F} = |\alpha|^2 e^{2r} + \sinh^2(r - z). \qquad (38)$$

FIG. 4. The phase sensitivity $\Delta\varphi$ versus the phase shift in the high-$|\alpha|$ regime ($|\alpha|^2 \gg \{\sinh^2\xi, \sinh^2\zeta\}$). The phase difference between the squeezers $\theta - \phi$ has a negligible impact on the QCRB but an important impact on the performance of realistic detection schemes. Parameters used: $|\alpha| = 10^3$, $\theta_\alpha = 0$, $r = 2.3$, $z = 2.2$, and $\theta = 0$. Inset: Zoom around $\varphi = \pi/2$ showing that the phase sensitivity in the difference-intensity detection scheme is indeed maximized for $\phi = \pi$.

But if we are in an experimentally interesting high-$|\alpha|$ regime, the effect is small. The question is now if this suboptimal PMC has any practical advantage.

In order to answer this question, the $\theta - \phi = 0/\pi$ scenarios are depicted in Fig. 4. One immediately notes that with the PMC from Eq. (37), $\Delta\varphi_{\text{hom}}$, $\Delta\varphi_{\text{df}}$, and $\Delta\varphi_{\text{sg}}$ are much more insensitive to the variation of φ. This is an experimental advantage, since a wider range of total internal phase shifts can be measured more accurately. Moreover, the single-intensity detection scheme shows much better results, this time the squeezing from port 1 showing its positive effect. This improvement can be traced back to the term $\Upsilon^-(\alpha, \zeta)$ that has been minimized this time to $|\alpha|^2 e^{-2z}$.

In Fig. 5 we discuss the same $\theta - \phi = 0/\pi$ problem at the optimal phase shift (φ_{opt}) for all considered detection schemes versus the QCRB. One notices that at low $|\alpha|$ the phase-matching condition $\theta - \phi = 0$ brings a significant penalty on both $\Delta\tilde{\varphi}_{\text{df}}$ (red curves) and $\Delta\varphi_{\text{QCRB}}$ (green curves). The phase-matching conditions (20) and (21) yield the best optimal phase sensitivity $\Delta\tilde{\varphi}_{\text{df}}$ throughout the whole range of $|\alpha|$. This is not true anymore for a single-mode intensity detection scheme (blue curves). Indeed, the aforementioned PMCs yield the best sensitivity only for $|\alpha| < |\alpha|_{\text{lim}}$, where we define

$$|\alpha|_{\text{lim}} = \frac{\sqrt{\cosh 2z + \sqrt{4\cosh^2 2z - 3}}}{2} \qquad (39)$$

and using the value of z used throughout this paper ($z = 2.2$) we find $|\alpha|_{\text{lim}} \approx 5.5$. For $|\alpha| > |\alpha|_{\text{lim}}$ the optimum PMCs are given by Eqs. (20) and (37) and the best achievable sensitivity for a single-mode intensity detection scheme is given by Eq. (D10). For even higher values of $|\alpha|$ the gap between the two performances increases in the favor of the PMC $\theta - \phi =$
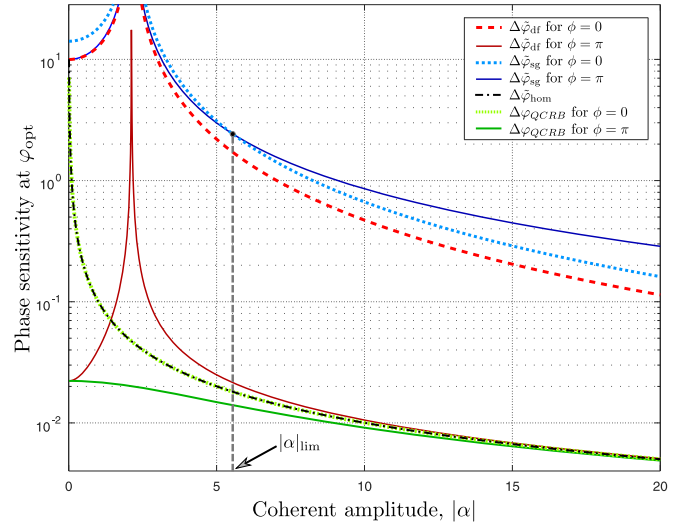

FIG. 5. The phase sensitivities $\Delta\tilde{\varphi}_{\text{df}}$, $\Delta\tilde{\varphi}_{\text{sg}}$, $\Delta\tilde{\varphi}_{\text{hom}}$, and $\Delta\varphi_{\text{QCRB}}$ versus the coherent amplitude $|\alpha|$. Parameters used: $\theta_\alpha = 0$, $r = 2.3$, $z = 2.2$, and $\theta = 0$.

0. Although not optimal, this detection scheme is experimentally interesting due to its simplicity and because the output port is "dark," thus extremely sensitive p-i-n photodiodes can be used. We can also point to the results of Ref. [22], where it has been shown that photon-number-resolving detection of only a small number of photons in the dark port can achieve the QCRB.

Except in the regime where $|\alpha| \ll \{\sinh^2 r, \sinh^2 z\}$ (where the difference-intensity detection scheme yields better results), the homodyne outperforms the other detection schemes considered. We mention that we have a single curve for $\Delta\tilde{\varphi}_{\text{hom}}$ in Fig. 5 because the phase sensitivity for a homodyne detection scheme at the optimum working point does not depend on the phase ϕ.

In the coherent plus squeezed vacuum scenario (i.e., for $z = 0$) the optimal PMC (20) is indisputable [7,9,37], most authors using it by default [5,11,20]. Adding squeezing to the coherent source from the input port 1 brought forward two scenarios. Indeed, the optimality given by the PMC from Eq. (21) is to be taken with a grain of salt. If one chases the ultimate bound on sensitivity, then the QFI from Eq. (22) and the related QCRB from Eq. (23) are the answer. If one is more interested in a wider range of φ while keeping a good sensitivity, then the PMCs (20) and (37) are more appropriate.

2. Nonunit photodetection efficiency

Losses inside the interferometer and due to the coupling with the environment are outside the scope of this paper. We point the interested reader to the available literature [38–40].

In Appendix C we briefly describe how to account for losses caused by nonunit photodetection efficiency (assumed identical to all detectors and modeled by the parameter $\eta \leqslant 1$, the ideal case implying $\eta = 1$). We begin with a single-mode intensity detection scheme and using Eq. (C3) we arrive at the
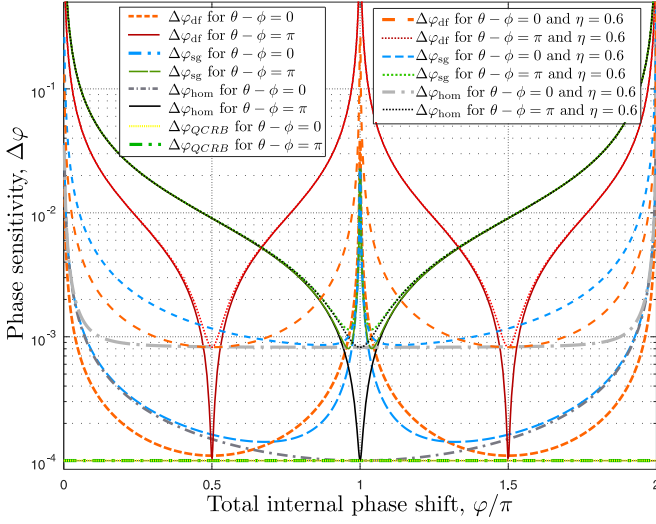
FIG. 6. The effect of nonunit photodetection efficiency on the phase sensitivity. While losses degrade the performance of all realistic scenarios, the PMC $\theta - \phi = 0$ still retains a better overall performance. Wherever not specified it is implied that $\eta = 1$. Parameters used: $|\alpha| = 10^3$, $r = 2.3$, $z = 2.2$, and $\theta_\alpha = \theta = 0$.

phase sensitivity

$$\Delta\varphi'_{\rm sg} = \frac{\sqrt{\Delta^2 \hat{n}_4 + \frac{1-\eta}{\eta}\langle \hat{n}_4 \rangle}}{|\partial_\varphi \langle \hat{n}_4 \rangle|}. \tag{40}$$

The numerator variance has the supplementary term $(1 - \eta)/\eta\langle \hat{n}_4 \rangle$. For a shot-noise limited detection (i.e., $\Delta^2 \hat{n}_4 = \langle \hat{n}_4 \rangle$) Eq. (40) reduces to $\Delta\varphi' = \Delta\hat{n}_4/(\sqrt{\eta}|\partial_\varphi \langle \hat{n}_4 \rangle|)$, a well-known result [40]. However the whole interest of squeezed states is to have $\Delta^2 \hat{n}_4 < \langle \hat{n}_4 \rangle$ and thus the addition of the $\langle \hat{n}_4 \rangle$ term is a clear degradation of the performance.

In Fig. 6 we plot the phase sensitivity for the ideal case ($\eta = 1$) as well as for the one including losses ($\eta = 0.6$). Although a swift degradation of the phase sensitivity in the case of PMC (37) is found, this setting yields still a better overall performance compared to the PMC (21).

The losses affect all considered realistic detection schemes. A general pattern emerges: the peak performance is the most affected and whatever the internal phase shift φ is we have $\Delta\varphi \leqslant \Delta\varphi'$. The experimentally preferable detection scheme emerges the homodyne detection due to its higher immunity to losses over a large range of internal phase shifts.

3. Phase-space representation and some physical insights

We give now a qualitative phase-space representation and some physical insights concerning the obtained results, especially the PMCs. In Fig. 7 (top left graphic) we have a standard phase-space representation of a coherent state (red circle) and a squeezed vacuum (green ellipse). Please note that the angle of rotation for the squeezed state is $\theta/2$, i.e., a rotation of $\theta = \pi$ brings the ellipse to a perpendicular position w.r.t. its original state [43,44]. The standard representation of a squeezed-coherent state is given in Fig. 7 (top right graphic).

However, in our interferometer, the coherent source α acts as a phase reference, therefore we have to rotate the phase
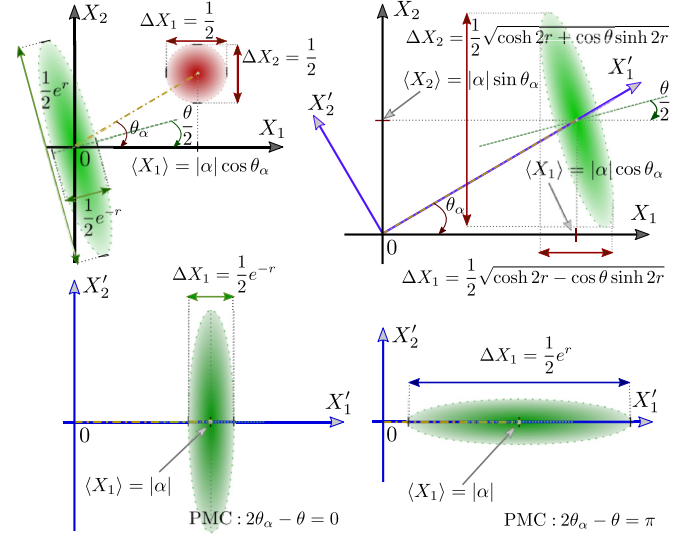

FIG. 7. Top left graphic: Phase-space representation of a coherent (red circle) and squeezed vacuum (green ellipse) states. Top right graphic: Standard phase-space representation of a squeezed-coherent state (see, e.g., Ref. [44], Sec. 5.6.). However, in the case of our interferometer, the phase reference is the coherent source α, therefore we rotate our measurement axis following θ_α (see blue axis, X'_1 and X'_2). Bottom left: Phase-space representation of a squeezed-coherent state in the rotated frame with PMC $2\theta_\alpha - \theta = 0$. Bottom right: Phase-space representation of a squeezed-coherent state in the rotated frame with PMC $2\theta_\alpha - \theta = \pi$.

space with θ_α (see blue axis in Fig. 7, top right graphic). This is what actually happens in the homodyne detection technique. The most important term determining the performance of $\Delta\hat{X}_{\phi_L} = \sqrt{\Delta^2 \hat{X}_{\phi_L}}$ from Eq. (32) is $\Upsilon^-(\alpha, \xi)$. The fact that $2\theta_\alpha - \theta = 0$ effectively squeezes the variance of $\Upsilon^-(\alpha, \xi)$, thus the average measured value is more accurate (see Fig. 7, bottom, left graphic).

We can extend the discussion to the difference- and single-mode detection techniques. The same term $\Upsilon^-(\alpha, \xi)$ is present in both Eqs. (25) and (29), thus the same PMC from Eq. (20) minimizes the respective variances, thus optimizing the phase sensitivity.

The fact that the squeezers have to be in antiphase was explained in the literature [6] (see also the discussion from Appendix E). Indeed, the optimal input state with two equal squeezed vacuums in antiphase ($\zeta = -\xi$) is an eigenvector of the beam splitter, i.e., the input state (16) becomes $|\psi'\rangle = \hat{D}_2(i\alpha/\sqrt{2})\hat{D}_3(\alpha/\sqrt{2})\hat{S}_2(-\xi)\hat{S}_3(\xi)|0\rangle$ after BS_1, result also reported in [48]. Thus, the same, unattenuated squeezing coefficient is available inside the interferometer.

At the same time with minimizing $\Upsilon^-(\alpha, \xi)$, one notes that $\Upsilon^+(\alpha, \xi)$ is maximized for $2\theta_\alpha - \theta = 0$. This fact is reassuring, since the Fisher information from Eq. (19) contains this term and we wish to have it maximized. Similarly, having the squeezers in antiphase changes the sign of the last term from Eq. (19), thus maximizing the Fisher information.

In the high-α regime, if we drop the insistence on having the squeezers in antiphase and the MZI is not operating at the optimum working point, another term, namely $\Upsilon^-(\alpha, \zeta)$, has to be minimized. Using the same arguments as before, leads us

to the condition $\theta - \phi = 0$. This gives a physical explanation for the PMC from Eq. (37).

4. Heisenberg scaling

We ponder now if a Heisenberg scaling [11,49] can be reached by an interferometer fed by the input state (16), i.e., if we can reach

$$\Delta\varphi_{HL} \approx \frac{1}{\langle N_{\text{tot}} \rangle}, \tag{41}$$

where $\langle N_{\text{tot}} \rangle = |\alpha|^2 + \sinh^2 r + \sinh^2 z$. Pezzé and Smerzi [20] showed that the scaling (41) can be reached by a coherent plus squeezed vacuum input if we consider $|\alpha|^2 \approx \sinh^2 r \approx \langle N_{\text{tot}} \rangle/2 \gg 1$. We denote $f_\alpha = |\alpha|^2/\langle N_{\text{tot}} \rangle$, $f_r = \sinh^2 r/\langle N_{\text{tot}} \rangle$, $f_z = \sinh^2 z/\langle N_{\text{tot}} \rangle$, and assume $\{|\alpha|^2, \sinh^2 r, \sinh^2 z\} \gg 1$. From Eq. (22) we obtain the Fisher information $\mathcal{F} \approx 4\langle N_{\text{tot}} \rangle^2 f_r (f_\alpha + f_z)$, hence the scaling

$$\Delta\varphi_{HL} \approx \frac{1}{\sqrt{4\langle N_{\text{tot}} \rangle^2 f_r (1 - f_r)}}. \tag{42}$$

The optimum is obtained when $f_r = 1/2$ yielding the QFI $\mathcal{F} = \langle N_{\text{tot}} \rangle^2$ and thus Heisenberg scaling from Eq. (41). Similar to the result from Ref. [20], half of the input power has to go into the squeezing from port 0 in order to guarantee a Heisenberg scaling. However, surprisingly, the limit (42) does not depend on f_α and f_z. Thus, the experimenter is free to choose the fraction of squeezed or coherent power in input port 1 at its own will (as long as $f_\alpha + f_z = 1/2$), while being guaranteed to reach a Heisenberg scaling.

The aforementioned Heisenberg scaling assumed the PMCs given by Eqs. (20) and (21). If we use instead the constraint (37), we arrive at the QFI given by Eq. (38) therefore $\mathcal{F} \approx 4\langle N_{\text{tot}} \rangle^2 f_\alpha f_r$. This time the Heisenberg scaling (41) imposes $f_\alpha = f_r \to 1/2$ (and consequently $f_z \to 0$), thus the optimum is found for a coherent plus squeezed vacuum input with half of the power denoted to squeezing [20].

IV. SQUEEZED-COHERENT PLUS SQUEEZED-COHERENT INPUT STATE

In this scenario we consider the most general Gaussian input state, namely a squeezed-coherent plus squeezed-coherent input,

$$|\psi_{\text{in}}\rangle = |(\alpha\zeta)_1(\beta\xi)_0\rangle = \hat{D}_1(\alpha)\hat{S}_1(\zeta)\hat{D}_0(\beta)\hat{S}_0(\xi)|0\rangle. \tag{43}$$

We impose for the time being no restriction on any of the parameters involved in this state.

Due to the number of variables, this scenario is more difficult to tackle. We start our discussion with the QFI and use it as a guide in order to be able to evaluate how well realistic detection schemes behave.

A. Fisher information and the Cramér-Rao bound

The Fisher matrix coefficients $\mathcal{F}_{ss}$, $\mathcal{F}_{dd}$, and $\mathcal{F}_{sd}$ are computed in Appendix F 1. In order to minimize the QCRB, one wishes to maximize the QFI given by Eq. (12). However, this time the problem is less trivial. In Sec. III the maximization of the QFI gave the phase-matching conditions (20) and (21).
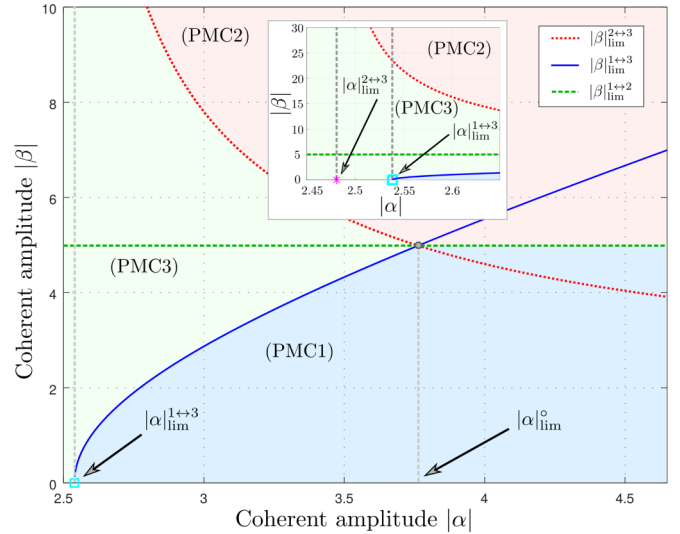

FIG. 8. All the optimum PMCs versus the input coherent amplitudes $|\alpha|$ and $|\beta|$ summarized in a graphical manner. The low-$|\alpha|$ coherent amplitude regime is depicted in the inset. With the squeezing factors $r = 2.3$ and $z = 2.2$ we get the limit values: $|\alpha|_{\text{lim}}^{1\leftrightarrow3} \approx 2.54$, $|\alpha|_{\text{lim}}^{2\leftrightarrow3} \approx 2.48$, $|\alpha|_{\text{lim}}^{\circ} \approx 3.76$, and $|\beta|_{\text{lim}}^{1\leftrightarrow2} \approx 4.98$.

Moreover, the phase-matching conditions did not depend on the values of the parameters involved, i.e., the amplitude of the coherent sources and the squeezing factor(s). This assertion is no longer true in the squeezed-coherent plus squeezed-coherent scenario.

Throughout our discussion, without loss of generality, we consider the coherent source $|\alpha|$ the primary one, thus, if necessary, the maximization of the coefficient $\Upsilon^+(\alpha, \xi)$ is privileged over the maximization of $\Upsilon^+(\beta, \zeta)$. The discussion is, of course, symmetric and one can switch $\alpha \leftrightarrow \beta$ and conduct a similar analysis. In this section we first present the phase-matching conditions leading to the optimal QFI and later we will justify them (see also the discussion from Appendix F 2). Throughout the discussion we fix the squeezing factors r and z and vary the coherent amplitudes. Thus, all the "limit values" ($|\alpha|_{\text{lim}}$ and $|\beta|_{\text{lim}}$) that will appear in our analysis will be functions of r and z. Please note that the values of r and z are in no way constrained.

Intense computer simulations showed that the Fisher information is maximized only by the PMCs $\theta_\alpha - \theta_\beta = n\pi/2$, $2\theta_\alpha - \theta = n'\pi$, and $2\theta_\beta - \phi = n''\pi$ with $n, n', n'' \in \mathbb{Z}$. This result constrained substantially our search for the optimum input PMCs.

We start from the PMCs (20) and (21) from Sec. III and add the condition (F8) on θ_β. We obtain the first set of input phase-matching conditions,

$$(\text{PMC1}) \begin{cases} 2\theta_\alpha - \theta = 0, \\ \phi - \theta = \pm\pi, \\ \theta_\alpha - \theta_\beta = 0. \end{cases} \tag{44}$$

These PMCs applied to Eq. (F7) give the QFI

$$\mathcal{F} = |\alpha|^2 e^{2r} + |\beta|^2 e^{-2z} + \sinh^2(r + z). \tag{45}$$

For $\{|\alpha|^2, \sinh^2 r, \sinh^2 z\} \gg |\beta|^2$ this QFI is obviously optimal (see also Fig. 8, blue shaded area). However, when

$|\beta|$ becomes comparable to $|\alpha|$, this is clearly not the case anymore. We thus impose a different set of phase-matching conditions when $\{|\alpha|^2, |\beta|^2\} \gg \{\sinh^2 r, \sinh^2 z\}$,

$$(\text{PMC2}) \begin{cases} 2\theta_\alpha - \theta = 0, \\ \phi - \theta = 0, \\ \theta_\alpha - \theta_\beta = 0, \end{cases} \tag{46}$$

that applied to Eq. (F7) give the QFI

$$\mathcal{F} = |\alpha|^2 e^{2r} + |\beta|^2 e^{2z} + \sinh^2(r - z). \tag{47}$$

This time the gain in the second term is accompanied by a less important contribution from the two squeezers. Comparing Eqs. (45) and (47) yields the limit value of $|\beta|$,

$$|\beta|_{\text{lim}}^{1\leftrightarrow 2} = \sqrt{\frac{\cosh 2r}{2}} \tag{48}$$

Thus, above a certain limit value of $|\alpha|$ [denoted $|\alpha|_{\text{lim}}^\circ$, to be specified shortly, see Eq. (55) and also Fig. 8], if $|\beta| < |\beta|_{\text{lim}}^{1\leftrightarrow 2}$, the QFI from Eq. (45) is maximal and the optimal PMCs are given by Eq. (44). If $|\beta| > |\beta|_{\text{lim}}^{1\leftrightarrow 2}$, the QFI from Eq. (47) is maximal and Eq. (46) gives the optimum PMCs (see also Fig. 8, red shaded area).

We introduce now the third and final set of phase-matching conditions,

$$(\text{PMC3}) \begin{cases} 2\theta_\alpha - \theta = 0, \\ 2\theta_\beta - \phi = 0, \\ \theta_\alpha - \theta_\beta = \frac{\pi}{2}, \end{cases} \tag{49}$$

that applied to Eq. (F7) give the Fisher information

$$\mathcal{F} = |\alpha|^2 e^{2r} + |\beta|^2 e^{2z} + \sinh^2(r + z)$$
$$- \frac{|\alpha\beta|^2 (e^{2r} + e^{2z})^2}{\frac{\sinh^2 2r}{2} + |\beta|^2 e^{2r} + \frac{\sinh^2 2z}{2} + |\alpha|^2 e^{2z}}. \tag{50}$$

As we will show, (PMC3) is optimal in the limit $\{\sinh^2 r, \sinh^2 z\} \gg \{|\alpha|^2, |\beta|^2\}$ (see also Fig. 8, green shaded area).

We need to find now the limit values of $|\alpha|$ and $|\beta|$ (themselves functions of the squeezing parameters r and z) that make the transition from one PMC to another. Without loss of generality, we fix the values $|\alpha|_{\text{lim}}$ and write $|\beta|_{\text{lim}}$ as functions of $|\alpha|_{\text{lim}}$. If a value $|\alpha|_{\text{lim}}$ makes the transition between, e.g., (PMC1) and (PMC2), it will be denoted by $|\alpha|_{\text{lim}}^{1\leftrightarrow 2}$, etc.

We first consider the low-$|\alpha|$ regime. Imposing equal Fisher information to Eqs. (45) and (50) (as $|\beta| \to 0$), we get the limit amplitude

$$|\alpha|_{\text{lim}}^{1\leftrightarrow 3} = \sqrt{\frac{2S \sinh 2z}{e^{2r}(e^{2r} + 2e^{2z}) + 1}}, \tag{51}$$

where $S = (\sinh^2 2r + \sinh^2 2z)/2$. With the values taken throughout this paper ($r = 2.3$, $z = 2.2$), we obtain the limit value $|\alpha|_{\text{lim}}^{1\leftrightarrow 3} \approx 2.54$.

As $|\alpha|$ increases, we cannot disregard the scenario employing (PMC2) from Eq. (46). Comparing the QFI from Eqs. (47) and (50) we arrive at the limit value,

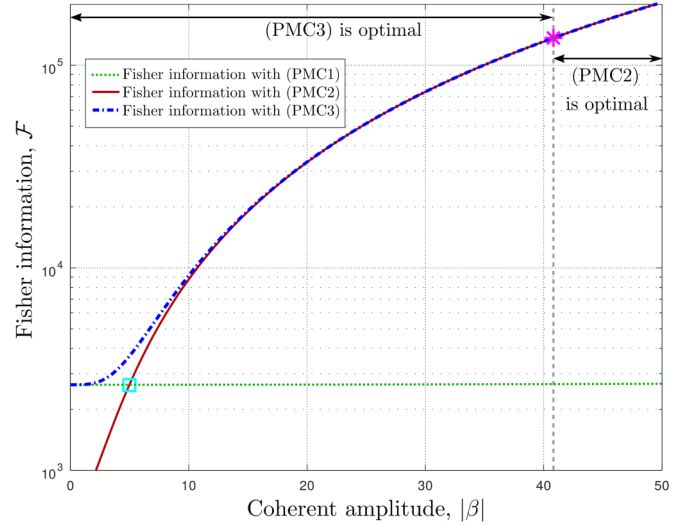$$|\alpha|_{\text{lim}}^{2\leftrightarrow 3} = e^{-z} \frac{\sqrt{\sinh 2r \sinh 2z}}{2\cosh(r - z)}. \tag{52}$$

FIG. 9. The QFI versus the coherent amplitude $|\beta|$ for $|\alpha| = 2.5$. Since $|\alpha| \in [|\alpha|_{\text{lim}}^{2\leftrightarrow 3}, |\alpha|_{\text{lim}}^{1\leftrightarrow 3}]$, the optimal input scenario is (PMC3) for $|\beta|$ smaller than $|\beta|_{\text{lim}}^{2\leftrightarrow 3}$ (magenta star) and (PMC2) thereafter. Parameters used: $r = 2.3$ and $z = 2.2$.

With the above values of r and z, we find $|\alpha|_{\text{lim}}^{2\leftrightarrow 3} \approx 2.48$.

Since we have now the two limit values $|\alpha|_{\text{lim}}^{1\leftrightarrow 3}$ and $|\alpha|_{\text{lim}}^{2\leftrightarrow 3}$, we can vary the parameter $|\alpha|$ from zero to arbitrary large values and search for the limit values of $|\beta|$. Thus, if $|\alpha| \in [|\alpha|_{\text{lim}}^{2\leftrightarrow 3}, |\alpha|_{\text{lim}}^{1\leftrightarrow 3}]$ we introduce the limit value of $|\beta|$,

$$|\beta|_{\text{lim}}^{2\leftrightarrow 3} = \sqrt{\frac{e^{2r} \sinh 2r \sinh 2z(|\alpha|^2 e^{2z} + S)}{4|\alpha|^2 e^{2z} \cosh^2(r - z) - \sinh 2r \sinh 2z}}. \tag{53}$$

We recall that $|\beta|_{\text{lim}}^{2\leftrightarrow 3}$ is a function of $|\alpha|$ (see also Fig. 8). For $|\beta| \leqslant |\beta|_{\text{lim}}^{2\leftrightarrow 3}$ the optimal QFI is obtained by imposing (PMC3) given by Eq. (49). If $|\beta| > |\beta|_{\text{lim}}^{2\leftrightarrow 3}$ the optimum is (PMC2) given by Eq. (46). This scenario is depicted in Fig. 9 (see also the inset from Fig. 8).

Satisfying the condition $|\alpha| \leqslant |\alpha|_{\text{lim}}^{1\leftrightarrow 3}$ guarantees that for very small $|\beta|$, (PMC3) from Eq. (49) is always optimal. If $|\alpha| > |\alpha|_{\text{lim}}^{1\leftrightarrow 3}$, this is no longer true. We introduce now the limit value,

$$|\beta|_{\text{lim}}^{1\leftrightarrow 3} = e^{z-r} \sqrt{|\alpha|^2 \left(\frac{2e^{2r} \cosh^2(r - z)}{\sinh 2z} - 1\right) - \frac{S}{e^{2z}}}. \tag{54}$$

For $|\alpha| > |\alpha|_{\text{lim}}^{1\leftrightarrow 3}$ as $|\beta|$ starts to grow from 0, (PMC1) from Eq. (44) will yield the maximum Fisher information until $|\beta| = |\beta|_{\text{lim}}^{1\leftrightarrow 3}$. At this point both scenarios yield the same Fisher information.

It can be shown that there exists a limit value $|\alpha| = |\alpha|_{\text{lim}}^\circ$ s. t. $|\beta|_{\text{lim}}^{1\leftrightarrow 2} = |\beta|_{\text{lim}}^{1\leftrightarrow 3} = |\beta|_{\text{lim}}^{2\leftrightarrow 3}$ and we find

$$|\alpha|_{\text{lim}}^\circ = \sqrt{\frac{e^{2r} \cosh 2r \sinh 2z + 2S}{e^{2r}(e^{2r} + 2e^{2z}) + 1}}. \tag{55}$$

For the parameters used we have $|\alpha|_{\text{lim}}^\circ \approx 3.76$. For $|\alpha| > |\alpha|_{\text{lim}}^\circ$ we are in a strong coherent regime. The optimum PMCs are to be chosen between (PMC1) and (PMC2) with a threshold given by $|\beta|_{\text{lim}}^{1\leftrightarrow 2}$, as mentioned before.
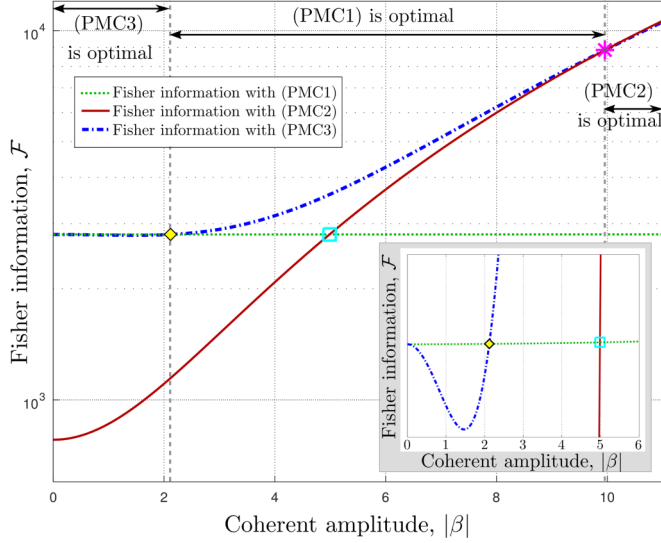
FIG. 10. The QFI versus the coherent amplitude $|\beta|$ for $|\alpha| = 2.8$. For $|\beta|$ smaller than $|\beta||_{\text{lim}}^{1\leftrightarrow3}$ (yellow diamond) (PMC3) is optimal while for $|\beta|$ bigger than $|\beta||_{\text{lim}}^{2\leftrightarrow3}$ (magenta star) (PMC2) yields the best performance. In between these values (PMC1) is optimal. Inset: Zoom on the range $|\beta| \in [0, 6]$. Parameters used: $r = 2.3$ and $z = 2.2$.

Thus, if $|\alpha| < |\alpha||_{\text{lim}}^{\circ}$ we have $|\beta||_{\text{lim}}^{1\leftrightarrow3} < |\beta||_{\text{lim}}^{1\leftrightarrow2} < |\beta||_{\text{lim}}^{2\leftrightarrow3}$, see Fig. 8. This scenario is also depicted in Fig. 10. For $|\beta| \leqslant |\beta||_{\text{lim}}^{1\leftrightarrow3}$ we have the optimum QFI given by (PMC1) from Eq. (44). For $|\beta| \in [|\beta||_{\text{lim}}^{1\leftrightarrow3}, |\beta||_{\text{lim}}^{2\leftrightarrow3}]$ the optimum is given by (PMC3) from Eq. (49) while for $|\beta| > |\beta||_{\text{lim}}^{2\leftrightarrow3}$ the optimum is given by (PMC2) from Eq. (46).

For $|\alpha| \geqslant |\alpha||_{\text{lim}}^{\circ}$ we have $|\beta||_{\text{lim}}^{2\leftrightarrow3} \leqslant |\beta||_{\text{lim}}^{1\leftrightarrow2} \leqslant |\beta||_{\text{lim}}^{1\leftrightarrow3}$ (see also Fig. 8). This scenario is depicted in Fig. 11. It corresponds to a higher power regime for the coherent sources w.r.t. the squeezing, therefore it is expected that (PMC3) from Eq. (49)
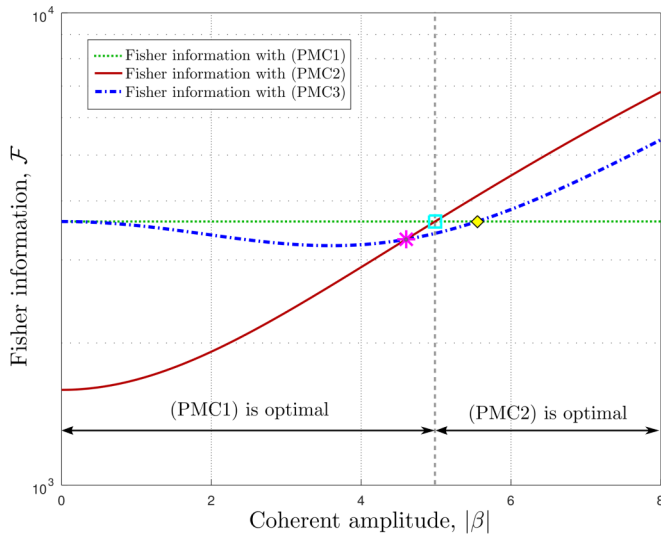

FIG. 11. The QFI versus the coherent amplitude $|\beta|$ for $|\alpha| = 4$. For $|\beta| \leqslant |\beta||_{\text{lim}}^{1\leftrightarrow2}/|\beta| > |\beta||_{\text{lim}}^{1\leftrightarrow2}$ (PMC1)/(PMC2) is optimal. The cyan square marks $|\beta||_{\text{lim}}^{1\leftrightarrow2}$ given by Eq. (48). Parameters used: $r = 2.3$, $z = 2.2$.
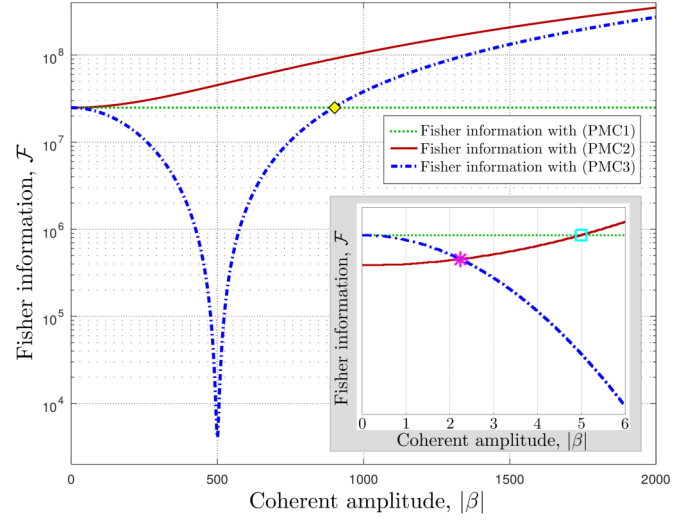

FIG. 12. The QFI versus the coherent amplitude $|\beta|$ for $|\alpha| = 500$. (PMC1) is optimal for $|\beta|$ below $|\beta||_{\text{lim}}^{1\leftrightarrow2}$ (cyan square) while above this value (PMC2) is preferred. Inset: Zoom on the range $|\beta| \in [0, 6]$. Parameters used $r = 2.3$, $z = 2.2$.

will lose the upper hand. Indeed for $|\beta| < |\beta||_{\text{lim}}^{1\leftrightarrow2}$ (PMC1) yields the maximum QFI while for $|\beta| > |\beta||_{\text{lim}}^{1\leftrightarrow2}$ (PMC2) is optimal.

This state of fact does not alter for high values of the coherent amplitudes. In Fig. 12 the QFI is depicted for three input phase-matching scenarios. There is no qualitative difference between the behavior in this case and in the one depicted in Fig. 11. The remarkable dip in the Fisher information corresponding to (PMC3) for $|\beta| \approx |\alpha|$ can be explained using the double-coherent scenario discussed in Refs. [7,9]. Indeed, since $\{|\alpha|, |\beta|\} \gg \{\sinh r, \sinh z\}$, we can approximate this situation with a double coherent input with PMC $\theta_\alpha - \theta_\beta = \pi/2$, yielding the minimal QFI (see, e.g., Eq. (12) in Ref. [9]).

We are able now to briefly discuss the case $|\alpha||_{\text{lim}}^{2\leftrightarrow3} > |\alpha||_{\text{lim}}^{1\leftrightarrow3}$. Indeed, considering the inset of Fig. 8, for $|\alpha| \in [|\alpha||_{\text{lim}}^{1\leftrightarrow3}, |\alpha||_{\text{lim}}^{2\leftrightarrow3}]$ one can see that instead of having the optimal (PMC3) for $|\beta| \leqslant |\beta||_{\text{lim}}^{2\leftrightarrow3}$, we have (PMC1) optimal for $|\beta| \leqslant |\beta||_{\text{lim}}^{1\leftrightarrow3}$ and (PMC3) for $|\beta| > |\beta||_{\text{lim}}^{1\leftrightarrow3}$. The rest of the discussion does not change.

To conclude, in a low-coherent scenario (i.e., when $\{|\alpha|, |\beta|\} \ll \{\sinh r, \sinh z\}$), (PMC3) yields the optimum QFI. Intuitively this can be explained by the fact that the most important term from Eq. (F5) in this regime is the third one. (PMC3) ensures that it is maximized and it manages to maximize the other two terms. This happens however with the price of having $\mathcal{F}_{sd} \neq 0$. Why (PMC3) is still optimal for $|\alpha|$ small but $|\beta|$ arbitrarily large can be explained by rewriting the phase-matching conditions as $2\theta_\beta - \phi = 0$ and $\theta - \phi = \pm\pi$ ($|\alpha|$ being small, θ_α is disregarded). We recognize here the squeezed-coherent plus squeezed vacuum scenario discussed in Sec. III, however with the input ports inverted.

As $|\alpha|$ grows there is a transition regime with various interplays between (PMC1) and (PMC3) for low $|\beta|$. For high $|\beta|$, (PMC2) is optimal.

In the high $|\alpha|$ regime (i.e., for $|\alpha| \geqslant |\alpha|_{\lim}^{\circ}$), for very low $|\beta|$, (PMC1) shortly dominates but as $|\beta|$ increases (PMC2) takes over.

B. Difference intensity detection scheme

From Eq. (6) and using the input state (43) we have the average of the observable $\hat{N}_d$,

$$\langle \hat{N}_d \rangle = \cos \varphi (|\alpha|^2 - |\beta|^2 + \sinh^2 z - \sinh^2 r)$$
$$- 2 \sin \varphi |\alpha \beta| \cos(\theta_\alpha - \theta_\beta). \quad (56)$$

The variance of $\hat{N}_d$ has been calculated in Appendix F [Eq. (F10)], and the phase sensitivity is given by Eq. (F11).

Similar to the previous sections an optimal total internal phase shift $\Delta \tilde{\varphi}_{df}$ can be computed and is formally given in Eq. (F13).

C. Single-mode intensity detection scheme

The average value of the operator $\hat{N}_4$ with the input state (43) is found to be

$$\langle \hat{N}_4 \rangle = \sin^2 \left(\frac{\varphi}{2} \right) (|\beta|^2 + \sinh^2 r)$$
$$+ \cos^2 \left(\frac{\varphi}{2} \right) (|\alpha|^2 + \sinh^2 z)$$
$$- \sin \varphi |\alpha \beta| \cos(\theta_\alpha - \theta_\beta) \quad (57)$$

and the absolute value of its derivative w.r.t. φ is

$$\left| \frac{\partial \langle \hat{N}_4 \rangle}{\partial \varphi} \right| = \left| \frac{1}{2} \sin \varphi (|\alpha|^2 + \sinh^2 z - |\beta|^2 - \sinh^2 r) \right.$$
$$\left. + \cos \varphi |\alpha \beta| \cos(\theta_\alpha - \theta_\beta) \right|. \quad (58)$$

The variance $\Delta^2 \hat{N}_4$ is calculated and given in Eq. (F14). The phase sensitivity $\Delta \varphi$ is also computed and given by Eq. (F15).

D. Homodyne detection scheme

Using Eq. (B5) and setting again $\phi_L - \theta_\alpha = 0$, we have

$$\left| \frac{\partial}{\partial \varphi} \langle \hat{X}_{\phi_L} \rangle \right| = \frac{1}{2} \left| \cos \left(\frac{\varphi}{2} \right) |\beta| \cos(\theta_\beta - \theta_\alpha) + \sin \left(\frac{\varphi}{2} \right) |\alpha| \right|. \quad (59)$$

The variance of $\hat{X}_{\phi_L}$ is computed using Eq. (B6) and yields the same result from Eq. (32). The phase sensitivity is thus given by

$$\Delta \varphi_{hom} = \frac{\sqrt{\cot^2 \left(\frac{\varphi}{2} \right) \Upsilon^-(\alpha, \zeta) + \Upsilon^-(\alpha, \xi)}}{|\alpha| \left| \cot \left(\frac{\varphi}{2} \right) |\beta| \cos(\theta_\beta - \theta_\alpha) + |\alpha| \right|}. \quad (60)$$

The optimum working point is found to be

$$\varphi_{opt} = 2 \arctan \left(\frac{|\alpha| \Upsilon^-(\alpha, \zeta)}{|\beta| \cos(\theta_\beta - \theta_\alpha) \Upsilon^-(\alpha, \xi)} \right), \quad (61)$$

yielding the best phase sensitivity

$$\Delta \tilde{\varphi}_{hom} = \frac{\sqrt{\Upsilon^-(\alpha, \xi) \Upsilon^-(\alpha, \zeta)}}{|\alpha| \sqrt{|\beta|^2 \cos^2(\theta_\alpha - \theta_\beta) \Upsilon^-(\alpha, \xi) + |\alpha|^2 \Upsilon^-(\alpha, \zeta)}}. \quad (62)$$
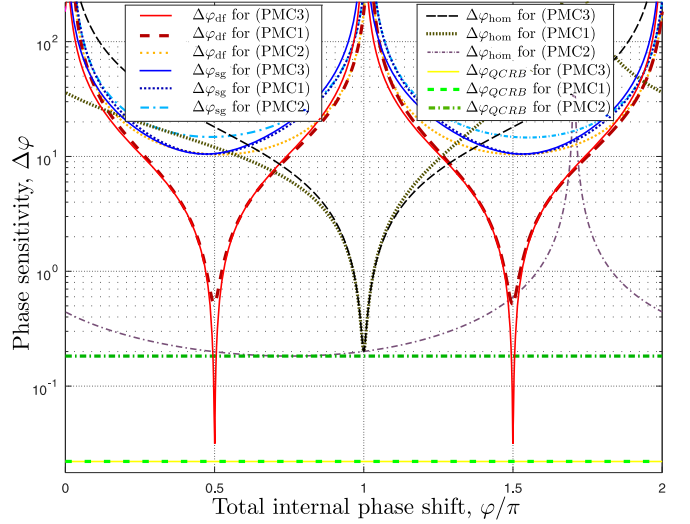

FIG. 13. Phase sensitivity versus the phase shift at low coherent amplitudes. Parameters used: $|\alpha| = 0.5$, $|\beta| = 0.25$, $r = 2.3$, and $z = 2.2$. As expected, for the low-intensity regime, (PMC3) is optimal. All realistic detection schemes are suboptimal, with the difference-intensity detection scheme yielding the best performance.

Assuming now that we are in the high-coherent regime, we impose (PMC2) from Eq. (46) and find the optimal phase sensitivity

$$\Delta \tilde{\varphi}_{hom} = \frac{1}{\sqrt{|\alpha|^2 e^{2r} + |\beta|^2 e^{2z}}}. \quad (63)$$

E. Discussion

1. Analysis of the obtained results

In Sec. IV A we concluded that the phase-matching condition (PMC3) given by Eq. (49) yields the maximum QFI in the low coherent amplitude regime. We depict this scenario in Fig. 13 both for the QCRB and realistic detection schemes. Indeed, one notes that the best performance for a difference-intensity detection scheme is obtained using (PMC3) from Eq. (49). For a single-mode intensity detection scheme, though, all input phase-matching conditions yield poor results. Equally noteworthy is the substantial suboptimality of the homodyne detection scheme w.r.t. the QCRB.

In Sec. IV A we concluded, too, that the best performance in the high-coherent regime is obtained by employing (PMC2) from Eq. (46). This also applies for realistic detection schemes, as depicted in Fig. 14. This time, the best performance is given by the homodyne detection technique. Noteworthy, each detection scheme yields its best sensitivity at a different optimal phase shift φ_{opt}.

From Eqs. (47) and (63) we see that in the high-coherent regime, the homodyne can actually reach the QCRB if $r = z$ and we have

$$\Delta \tilde{\varphi}_{hom} = \frac{e^{-r}}{\sqrt{|\alpha|^2 + |\beta|^2}} = \Delta \varphi_{QCRB}. \quad (64)$$

We conclude that for (PMC2) the optimal input state is the one with equal squeezing factors in both input ports.
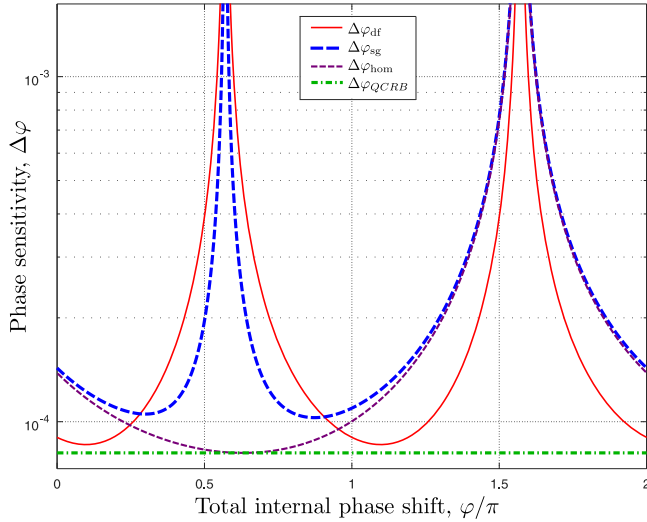
FIG. 14. Phase sensitivity for a squeezed-coherent plus squeezed-coherent input versus the phase at high coherent amplitudes with (PMC2). Parameters used: $|\alpha| = 1000$, $|\beta| = 800$, $r = 2.3$, and $z = 2.2$.

We ask now the question: could we have an experimental advantage if we start from a squeezed-coherent plus squeezed vacuum input as discussed in Sec. III and add some limited displacement to the squeezed vacuum from port 1 (i.e., we have $|\beta| \ll |\alpha|$)? The answer is affirmative and we depict this scenario in Fig. 15. Indeed, for $\beta = 0$ we find the result discussed in Sec. III and depicted in Fig. 4 (solid red curve). The difference-intensity detection scenario has a very peaked optimum at $\varphi_{\rm opt} = \pi/2$. As $|\beta|$ starts to grow, the shape of the phase sensitivity is simply translated. Therefore, instead of having a very good phase sensitivity only around $\varphi \approx \pi/2$, we can scan other internal phase shifts by simply manipulating $|\beta|$. Please note the we are in the (PMC1) regime and we assume $|\beta| \ll |\alpha|$. The addition of the second coherent source
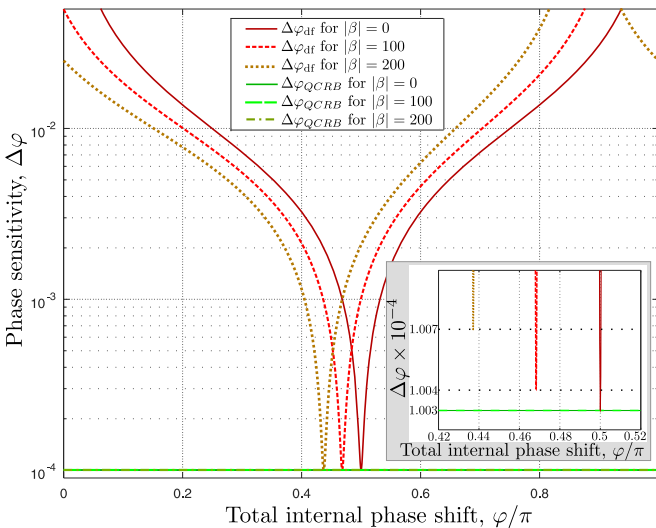

FIG. 15. Phase sensitivity for $|\alpha| = 10^3$ and a small $|\beta|$. The (PMC1) constraints are used. Inset: Extreme zoom in the region $\varphi \in [0.42\pi, 0.52\pi]$. Parameters used: $r = 2.3$ and $z = 2.2$.
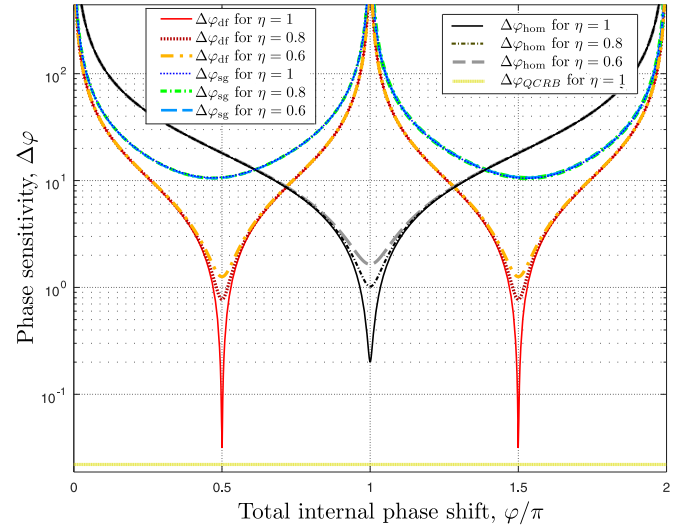

FIG. 16. The effect of nonunit photodetection efficiency on the phase sensitivity for a squeezed-coherent plus squeezed-coherent input. A sensible degradation in performance is noticeable especially at the peaks of sensitivity. Being in the low-coherent region, (PMC3) is employed. Parameters used: $|\alpha| = 0.5$, $|\beta| = 0.25$, $r = 2.3$, and $z = 2.2$.

negligibly degrades the performance, as seen in the inset of Fig. 15.

2. Nonunit photodetection efficiency

In this section we use results from Appendix C as well as Eq. (40).

In Fig. 16 we single out (PMC3) from Fig. 13 and evaluate the effect of nonunit photodetection efficiencies. The most noticeable effect is the swift degradation of the peaks of sensitivity for the difference-intensity and homodyne detection schemes. The single-mode intensity detection performance is the least affected by the effect of losses, however this is also due to the poor performance of this detection strategy, given the parameters used in Fig. 16.

In Fig. 17 a high-$|\alpha|$ scenario employing (PMC1) is depicted (see also Fig. 15 for the loss-less case). This time the effect of nonunit photodetection efficiency is noticeable for all realistic detection schemes, with a remark similar to the one from Sec. III E namely that the respective sensitivity peaks are the most impacted by the losses.

3. A physical insight on the obtained phase-matching conditions

We give now some physical insights on the obtained results. For (PMC1) we point the reader to the discussion from Sec. III E. As mentioned before, β is mainly a degrading factor of the overall performance, thus its interest lies only in the regime $|\beta| \ll |\alpha|$.

The experimentally interesting high-coherent regime setup relies on (PMC2). In Refs. [7,9] it has been shown that maximum performance from a dual coherent input implies $\theta_\alpha = \theta_\beta$ (see also Fig. 18 for a graphical representation). In our setup, we have two extra squeezings, one in each port. At a careful look, in the case of (PMC2) we actually have twice a coherent plus squeezed vacuum input, namely
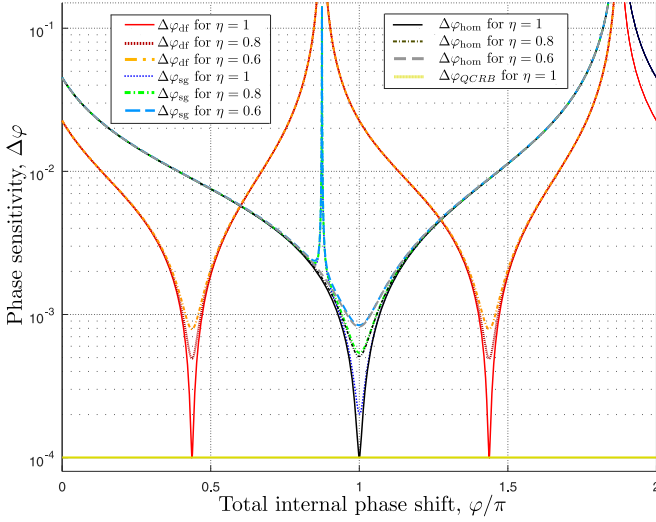
FIG. 17. The effect of nonunit photodetection efficiency on the phase sensitivity for a squeezed-coherent plus squeezed-coherent input. A sensible degradation in performance is found for all realistic detection schemes around their respective peak performance. (PMC1) is employed. Parameters used: $|\alpha| = 10^3$, $|\beta| = 200$, $r = 2.3$, and $z = 2.2$.

$\alpha - \xi$ and $\beta - \zeta$. The optimal PMC for each one implies a relation of the type (20). Indeed, setting $\alpha = \beta$ and $\xi = \zeta$ we get $\mathcal{F} = 2|\alpha|^2 e^{2r}$ which is twice the Fisher information for the coherent plus squeezed vacuum input (in the high-$|\alpha|$ approximation). These PMCs do minimize the term $\Upsilon^-(\alpha, \xi)$ from the homodyne sensitivity (60) and the term $\Upsilon^-(\beta, \zeta)$ from the difference-intensity detection sensitivity (F10). A supplementary justification for the QCRB optimality of this state can be found in the work of Hofmann ("path-symmetric states can achieve their quantum Cramer-Rao bound") [50].

One can argue that in (PMC2) we have $\xi = \zeta$ instead of $\xi = -\zeta$, thus a suboptimality should be expected from this scheme (see also the discussion from Appendix E). The argument is valid, however, (PMC2) is a high-coherent scheme,
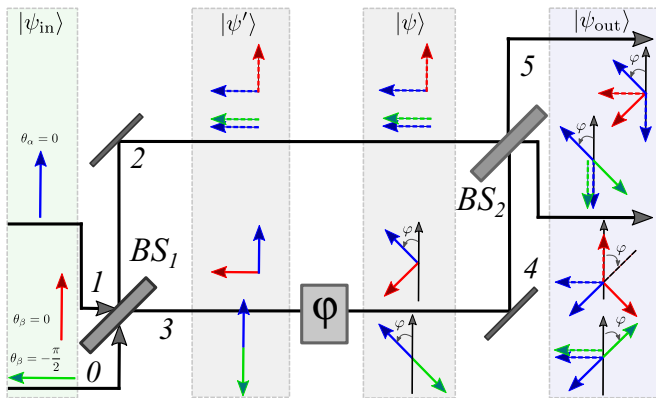

FIG. 18. A phasor representation of a double-coherent input MZI in two scenarios: (i) Both coherent inputs are in phase (red and blue arrows) and (ii) they are $\pi/2$ phase shifted (red and magenta arrows). For equal input amplitudes and (ii), ones notes that the outputs do not depend anymore on the angle φ.

i.e., $\{|\alpha|^2, |\beta|^2\} \gg \{\sinh^2 r, \sinh^2 z\}$, thus the nonoptimality from the interaction of the squeezed vacuums should be marginal.

Finally, (PMC3) starts by insisting on the squeezers being in antiphase. Assuming again $\zeta = -\xi$ we have the state after the beam splitter $|\psi'\rangle = \hat{D}_2[(i\alpha + \beta)/\sqrt{2}]\hat{D}_3[(\alpha + i\beta)/\sqrt{2}]\hat{S}_2(\xi)_2\hat{S}_3(-\xi)|0\rangle$ (see Appendix E). Since we have now $\theta_\alpha - \theta_\beta = \pi/2$ we obtain $\hat{D}_3[(\alpha + i\beta)/\sqrt{2}] = \hat{D}_3[e^{i\theta_\alpha}(|\alpha| - |\beta|)/\sqrt{2}]$ with a total annihilation of the coherent amplitude mode 3 for $|\alpha| = |\beta|$. This phenomenon can be easily represented graphically, as depicted in Fig. 18. The arrows represent the two input coherent states (α and β) and for $\theta_\alpha - \theta_\beta = \pi/2$ the amplitude in mode 3 inside the MZI destructively interferes while at the photodetectors, none of the outputs depends on the phase φ if $|\alpha| = |\beta|$.

One can use this argument to point to the suboptimality of (PMC3). As remarked in the case of (PMC2), one must also pay attention where the given PMCs apply. The destructive interference of the coherent sources inside the interferometer is a limited nuisance because in the case of (PMC3) we are in the low-coherent regime, $\{|\alpha|^2, |\beta|^2\} \ll \{\sinh^2 r, \sinh^2 z\}$. We actually rely here on the optimality of the squeezed vacuums. We can approximate the wave function after BS_1 with $|\psi'\rangle \approx \hat{S}_2(\xi)_2\hat{S}_3(-\xi)|0\rangle$ and, as discussed before, this is an optimal state [6].

4. Heisenberg scaling

We end this work by investigating the Heisenberg scaling (41) in the case of an input state given by Eq. (43). The total average number of input photons in this scenario is $\langle N_{\text{tot}}\rangle = |\alpha|^2 + |\beta|^2 + \sinh^2 r + \sinh^2 z$. We define $f_\alpha = |\alpha|^2/\langle N_{\text{tot}}\rangle$, $f_\beta = |\beta|^2/\langle N_{\text{tot}}\rangle$, $f_r = \sinh^2 r/\langle N_{\text{tot}}\rangle$, and $f_z = \sinh^2 z/\langle N_{\text{tot}}\rangle$. We again assume $\{|\alpha|^2, |\beta|^2, \sinh^2 r, \sinh^2 z\} \gg 1$. Since we did not in any way specify the relation among the squeezing factors and the coherent amplitudes, any among the phase-matching conditions discussed before could be optimal. We thus discuss them all and first consider (PMC1) and the QFI given by Eq. (45). We find $\mathcal{F} \approx 4\langle N_{\text{tot}}\rangle^2 f_r(f_\alpha + f_z)$, a result formally identical to the one obtained in Sec. III E. However, $\langle N_{\text{tot}}\rangle$ is now different and rewriting $\mathcal{F} \approx 4\langle N_{\text{tot}}\rangle^2 f_r(1 - f_r - f_\beta)$ we see that the optimum implies $f_\beta \to 0$ and $f_r \to 1/2$. This scenario does not exclude the constraint $f_\alpha \to 0$, thus also two squeezed vacuums can yield the scaling (41). By two "squeezed vacuums" here and in the following discussion we mean $\{|\alpha|^2, |\beta|^2\} \ll \{\sinh^2 r, \sinh^2 r\}$ thus, although we assumed $\{|\alpha|^2, |\beta|^2, \sinh^2 r, \sinh^2 z\} \gg 1$ we can safely approximate our input state with two squeezed vacuums.

For (PMC2) we have the QFI from Eq. (47). Assuming again $\{|\alpha|^2, |\beta|^2, \sinh^2 r, \sinh^2 z\} \gg 1$, we get

$$\mathcal{F} \approx 4\langle N_{\text{tot}}\rangle^2 (f_\alpha f_r + f_\beta f_z). \tag{65}$$

The optimum solution $\mathcal{F} \approx \langle N_{\text{tot}}\rangle^2$ is obtained in two scenarios: if $f_r \to 1/2$, $f_z \to 0$ and $f_\alpha \to 1/2$ (thus $f_\beta \to 0$) or if $f_r \to 0$, $f_z \to 1/2$ and $f_\beta \to 1/2$ (thus $f_\alpha \to 0$). This time the optimum involves either a coherent source in port 1 and squeezed vacuum in port 0 or a coherent source in port 0 and squeezed vacuum in port 1, thus excluding the two squeezed vacuums scenario from (PMC1). Why this is so, boils down to the insistence of (PMC2) on having the constraint $\theta - \phi = 0$.

For (PMC3) we have the QFI from Eq. (50). Assuming again $\{|\alpha|^2, |\beta|^2, \sinh^2 r, \sinh^2 z\} \gg 1$, we get

$$
\mathcal{F} \approx 4\langle N_{\text{tot}}\rangle^2 \bigg(f_\alpha f_r + f_\beta f_z + f_r f_z
$$
$$
- \frac{f_\alpha f_\beta (f_r + f_z)^2}{\frac{f_r^2}{2} + \frac{f_z^2}{2} + f_\alpha f_z + f_\beta f_r} \bigg). \quad (66)
$$

Somehow not surprisingly, the optimum $\mathcal{F} \approx \langle N_{\text{tot}}\rangle^2$ is obtained for $f_r = f_z \to 1/2$, thus the best scaling is obtained with two squeezed vacuums.

In conclusion, if we impose (PMC1) and $|\beta| \neq 0$, for a Heisenberg scaling the optimum involves (i) either a squeezed vacuum having half the input power in one port and a squeezed-coherent state in the other one or (ii) two squeezed vacuums and no coherent sources. This last result can be put in relation with a similar findings reported in the literature [6,51]. If we impose (PMC2) the optimal Heisenberg scaling is obtained by applying a coherent plus squeezed vacuum input. This result agrees with the conclusions from Ref. [5]. Finally, imposing (PMC3) and a Heisenberg scaling takes us again to the solution involving two squeezed vacuums.

We can also compare our results with the ones reported in Refs. [35,36]. For a squeezed-coherent plus squeezed-coherent input state, Sparaciari, Olivares, and Paris found the optimum QFI when $f_r = f_z \approx 1/3$ and $f_\alpha = f_\beta$ yielding a scaling $\mathcal{F} = 8/9\langle N_{\text{tot}}\rangle^2$. If we introduce these values in Eq. (65) we find $\mathcal{F} = 4/9\langle N_{\text{tot}}\rangle^2$. This discrepancy should come as no surprise: while in Refs. [35,36] the authors started from a single-parameter Fisher information, we started from a two-parameter Fisher information approach.

V. THE IMPACT OF THE BS TYPE EMPLOYED ON THE PHASE-MATCHING CONDITIONS

Up to this point we discussed the field operator transformations (2) characterizing a so-called balanced symmetrical or thin-film BS [43]. If we introduce the Jordan-Schwinger angular momentum operators [11,29,52] $\hat{J}_x = (\hat{a}_1^\dagger \hat{a}_2 + \hat{a}_1 \hat{a}_2^\dagger)/2$, $\hat{J}_y = (\hat{a}_1^\dagger \hat{a}_2 - \hat{a}_1 \hat{a}_2^\dagger)/2i$, and $\hat{J}_z = (\hat{a}_1^\dagger \hat{a}_1 - \hat{a}_2^\dagger \hat{a}_2)/2$, the transformation from Eq. (3) corresponds to the unitary transformation $\hat{U}_x = e^{i\pi/2\hat{J}_x}$. For example, we have $\hat{a}_2 = \hat{U}_x^\dagger \hat{a}_0 \hat{U}_x = 1/\sqrt{2}\hat{a}_0 + i/\sqrt{2}\hat{a}_1$. The same initial convention (2) determines the QFI matrix elements calculated in Appendix A and also the output operator transformations from Eq. (3) leading to the observables for the realistic schemes discussed in Appendix B.

However, there are nonsymmetric beam splitters (usually called "cube beam splitters") that are described by the field operator transformations [29]

$$
\hat{a}_3 = \frac{1}{\sqrt{2}}(\hat{a}_1 - \hat{a}_0),
$$
$$
\hat{a}_2 = \frac{1}{\sqrt{2}}(\hat{a}_1 + \hat{a}_0). \quad (67)
$$

These field operator transformations correspond to the unitary operator $\hat{U}_y = e^{i\pi/2\hat{J}_y}$. They imply the input-output field operator transformations

$$
\hat{n}_4 = \cos^2\left(\frac{\varphi}{2}\right)\hat{n}_1 + \sin^2\left(\frac{\varphi}{2}\right)\hat{n}_0 + \sin\varphi\,\mathrm{Im}(\hat{a}_1\hat{a}_0^\dagger) \quad (68)
$$

where Im denotes the imaginary part and

$$
\hat{N}_d = \cos\varphi(\hat{n}_1 - \hat{n}_0) + 2\sin\varphi\,\mathrm{Im}(\hat{a}_1\hat{a}_0^\dagger). \quad (69)
$$

If we compute now the Fisher matrix coefficients using Eq. (67) we get $\mathcal{F}_{ss} = \Delta^2\hat{n}_1 + \Delta^2\hat{n}_0$,

$$
\mathcal{F}_{dd} = \langle\hat{n}_1\rangle + \langle\hat{n}_0\rangle + 2(\langle\hat{n}_0\rangle\langle\hat{n}_1\rangle - |\langle\hat{a}_0\rangle|^2|\langle\hat{a}_1\rangle|^2)
$$
$$
+ 2\mathrm{Re}\{\langle\hat{a}_0^2\rangle\langle(\hat{a}_1^\dagger)^2\rangle - \langle\hat{a}_0\rangle^2\langle\hat{a}_1^\dagger\rangle^2\}, \quad (70)
$$

and the third Fisher matrix coefficient is

$$
\mathcal{F}_{sd} = 2\mathrm{Re}\{\langle\hat{a}_0\rangle\langle\hat{a}_1^\dagger\rangle + \langle\hat{a}_0\rangle(\langle\hat{a}_1^\dagger\hat{n}_1\rangle - \langle\hat{a}_1^\dagger\rangle\langle\hat{n}_1\rangle)
$$
$$
+ (\langle\hat{n}_0\hat{a}_0\rangle - \langle\hat{a}_0\rangle\langle\hat{n}_0\rangle)\langle\hat{a}_1^\dagger\rangle\}. \quad (71)
$$

Please note that in the calculation of the Fisher matrix element $\mathcal{F}_{ss}$ the new expressions for the output number operators have to be used, e.g., Eq. (68), etc. The optimum QFI as well as the best performance for realistic detection scenarios remain unchanged, however a new assessment of the input PMCs has to be done.

For example, if we consider the squeezed-coherent plus squeezed vacuum input state from Eq. (16) and a BS characterized by the transformation (67) we obtain the QFI (we recall that is in this scenario $\mathcal{F} = \mathcal{F}_{dd}$)

$$
\mathcal{F} = \Upsilon^-(\alpha, \xi)
$$
$$
+ \frac{\cosh 2r \cosh 2z + \sinh 2r \sinh 2z \cos(\theta - \phi) - 1}{2}. \quad (72)
$$

This time, contrary to the PMCs given by Eqs. (20) and (21) we find the optimal QFI (22) if

$$
2\theta_\alpha - \theta = \pm\pi,
$$
$$
\theta - \phi = 0. \quad (73)
$$

In a similar manner, all results discussed in Secs. III and IV can be rederived.

The physical origin of the sign change (w.r.t. the previous sections) in all terms involving fields from both inputs is easy to explain: while the field operator transformations from Eq. (2) describe a symmetrical BS, the ones from Eq. (67) do not. Indeed, in a cube beam splitter one mode propagates without phase shifts, while for the second one the reflection acquires a phase delay of π. One can also redraw the arrows from Fig. 18 by following the rules of the field operator transformations (67) and convince itself of the new optimal PMCs with a cube type BS.

VI. CONCLUSIONS

In this paper we investigated the phase sensitivity of a Mach-Zehnder interferometer fed with the most general Gaussian input states. Both the theoretical quantum Cramér-Rao bound and realistic performances were assessed.

The squeezed-coherent plus squeezed vacuum input state scenario yielded unambiguous phase-matching conditions for

a theoretical maximum performance. If the phase of the coherent source is taken to be zero, then the squeezing from the opposite input port has to be zero, too. However, the second squeezer must be in antiphase. We also showed that a second scenario is possible, when all input phases are zero. Although slightly suboptimal, this scenario has a good sensitivity over a wide range of internal phase shifts.

The paper discussed in detail the rather complicated case of squeezed-coherent plus squeezed-coherent input. We found three input phase-matching scenarios, each optimal in a certain domain. In the low coherent intensity regime, we found that the optimal input phase-matching condition involves the two coherent sources being dephased by $\pi/2$ and the squeezers in antiphase. In the high-coherent intensity regime, the optimal input phase-matching conditions impose the coherent sources as well as the squeezers to be in phase (if the coherent phases are assumed to be zero).

Practical situations have been discussed with realistic detection schemes, where the addition of the second coherent source is able to bring an experimental advantage. We also showed that with the right phase-matching conditions and with equal squeezing in both inputs, some realistic detection techniques are able to saturate the quantum Cramér-Rao bound.

When considering losses, all realistic detection schemes show a decrease in performance, the peak performance being the most affected. In most scenarios, the least impacted detection scheme in the lossy case is the homodyne detection. A more thorough investigation on the impact of the different types of losses on the interferometric phase sensitivity is postponed for a future work.

For all input states considered we showed that a Heisenberg scaling is possible. We also showed that in the case of a general Gaussian state, different PMCs lead to different input states that optimize the Heisenberg scaling, confirming, and extending some previous results.

We also discussed the impact of the type of beam splitter used. We showed that although the optimal phase sensitivity is unaffected by the type of the beam splitter used, the input phase-matching conditions needed to attain this optimum do change.

APPENDIX A: FISHER INFORMATION

Since we assume our input to be in a pure state, we do not need to use the symmetric logarithmic derivative [11,32,42] and the QFI is directly

$$\mathcal{F}(\varphi) = 4(\langle \partial_\varphi \psi | \partial_\varphi \psi \rangle - |\langle \partial_\varphi \psi | \psi \rangle|^2), \tag{A1}$$

where $|\partial_\varphi \psi\rangle = \partial|\psi\rangle/\partial\varphi$ [5–7,42]. To give a basic example for readers unfamiliar with this notation, if the wave function is $|\psi\rangle = \cos\varphi|0\rangle + \sin\varphi|1\rangle$, then we have $|\partial_\varphi \psi\rangle = -\sin\varphi|0\rangle + \cos\varphi|1\rangle$.

We consider the general case where each arm of the MZI contains a phase shift (φ_1 and, respectively, φ_2). The estimation is treated as a general two parameter problem [5–7,21]. We define the 2×2 Fisher information matrix:

$$\mathcal{F} = \begin{bmatrix} \mathcal{F}_{ss} & \mathcal{F}_{sd} \\ \mathcal{F}_{ds} & \mathcal{F}_{dd} \end{bmatrix}, \tag{A2}$$

where

$$\mathcal{F}_{ij} = 4\mathrm{Re}\{\langle \partial_i \psi | \partial_j \psi \rangle - \langle \partial_i \psi | \psi \rangle \langle \psi | \partial_j \psi \rangle\}, \tag{A3}$$

with $i, j \in \{s, d\}$ and $\varphi_{s/d} = (\varphi_1 \pm \varphi_2)/2$. From this matrix we arrive at the QCRB matrix inequality [5] out of which we retain only the difference-difference phase estimator,

$$(\Delta\varphi_d)^2 \geqslant (\mathcal{F}^{-1})_{dd}. \tag{A4}$$

Using the definition from (A3), the sum-sum Fisher matrix element $\mathcal{F}_{ss}$ can be computed and yields

$$\mathcal{F}_{ss} = \Delta^2 \hat{n}_0 + \Delta^2 \hat{n}_1. \tag{A5}$$

Similarly the element $\mathcal{F}_{dd}$ is computed and yields

$$\mathcal{F}_{dd} = \langle \hat{n}_1 \rangle + \langle \hat{n}_0 \rangle + 2(\langle \hat{n}_0 \rangle \langle \hat{n}_1 \rangle - |\langle \hat{a}_0 \rangle|^2 |\langle \hat{a}_1 \rangle|^2)$$
$$- 2\mathrm{Re}(\langle \hat{a}_0^2 \rangle \langle (\hat{a}_1^\dagger)^2 \rangle - \langle \hat{a}_0 \rangle^2 \langle \hat{a}_1^\dagger \rangle^2). \tag{A6}$$

The last term we need is $\mathcal{F}_{sd}$ since $\mathcal{F}_{sd} = \mathcal{F}_{ds}$ [5]. We have

$$\mathcal{F}_{sd} = 2\mathrm{Im}[\langle \hat{a}_0 \rangle \langle \hat{a}_1^\dagger \rangle + (\langle \hat{n}_0 \hat{a}_0 \rangle - \langle \hat{n}_0 \rangle \langle \hat{a}_0 \rangle)\langle \hat{a}_1^\dagger \rangle$$
$$+ \langle \hat{a}_0 \rangle (\langle \hat{a}_1^\dagger \hat{n}_1 \rangle - \langle \hat{a}_1^\dagger \rangle \langle \hat{n}_1 \rangle)]. \tag{A7}$$

APPENDIX B: CALCULATION OF THE OUTPUT VARIANCES FOR THE GENERIC CASE

In this Appendix we compute the averages $\langle \hat{N}^2 \rangle$ as well as the variances $\Delta^2 \hat{N}$ for a generic input case.

1. Difference intensity detection

For a difference intensity detection scheme, from Eqs. (3) and (5) we obtain the expression of $\hat{N}_d^2$ as a function of input operators. After a long but straightforward calculation we obtain the final expression

$$\langle \hat{N}_d^2 \rangle = \cos^2\varphi(\langle \hat{n}_0^2 \rangle + \langle \hat{n}_1^2 \rangle) - 2\cos(2\varphi)\langle \hat{n}_0 \hat{n}_1 \rangle$$
$$+ \sin^2\varphi(\langle \hat{n}_0 \rangle + \langle \hat{n}_1 \rangle + \langle \hat{a}_0^2 (\hat{a}_1^\dagger)^2 \rangle + \langle (\hat{a}_0^\dagger)^2 \hat{a}_1^2 \rangle)$$
$$+ \sin 2\varphi(\langle \hat{n}_0 \hat{a}_0 \hat{a}_1^\dagger \rangle + \langle \hat{a}_0^\dagger \hat{n}_0 \hat{a}_1 \rangle$$
$$- \langle \hat{a}_0 \hat{a}_1^\dagger \hat{n}_1 \rangle - \langle \hat{a}_0^\dagger \hat{n}_1 \hat{a}_1 \rangle). \tag{B1}$$

Since we expressly assume that the input state is *separable*, we can write

$$\langle \hat{N}_d^2 \rangle = \cos^2\varphi(\langle \hat{n}_0^2 \rangle + \langle \hat{n}_1^2 \rangle) - 2\cos(2\varphi)\langle \hat{n}_0 \rangle \langle \hat{n}_1 \rangle$$
$$+ \sin^2\varphi(\langle \hat{n}_0 \rangle + \langle \hat{n}_1 \rangle + \langle \hat{a}_0^2 \rangle \langle (\hat{a}_1^\dagger)^2 \rangle + \langle (\hat{a}_0^\dagger)^2 \rangle \langle \hat{a}_1^2 \rangle)$$
$$+ \sin 2\varphi(\langle \hat{n}_0 \hat{a}_0 \rangle \langle \hat{a}_1^\dagger \rangle + \langle \hat{a}_0^\dagger \hat{n}_0 \rangle \langle \hat{a}_1 \rangle$$
$$- \langle \hat{a}_0 \rangle \langle \hat{a}_1^\dagger \hat{n}_1 \rangle - \langle \hat{a}_0^\dagger \rangle \langle \hat{n}_1 \hat{a}_1 \rangle). \tag{B2}$$

The term $\langle\hat{N}_d\rangle^2$ can be computed from Eq. (6) and we find the variance

$$\Delta^2\hat{N}_d = \cos^2\varphi(\Delta^2\langle\hat{n}_0\rangle + \Delta^2\langle\hat{n}_1\rangle) + \sin^2\varphi\big[\langle\hat{n}_0\rangle + \langle\hat{n}_1\rangle + 2\langle\hat{n}_0\rangle\langle\hat{n}_1\rangle - 2|\langle\hat{a}_0\rangle|^2|\langle\hat{a}_1\rangle|^2 + 2\mathrm{Re}\big(\langle\hat{a}_0^2\rangle\langle(\hat{a}_1^\dagger)^2\rangle - \langle\hat{a}_0\rangle^2\langle\hat{a}_1^\dagger\rangle^2\big)\big]$$

$$+ 2\sin 2\varphi\mathrm{Re}[(\langle\hat{a}_0^\dagger\hat{n}_0\rangle - \langle\hat{n}_0\rangle\langle\hat{a}_0^\dagger\rangle)\langle\hat{a}_1\rangle - \langle\hat{a}_0\rangle(\langle\hat{a}_1^\dagger\hat{n}_1\rangle - \langle\hat{a}_1^\dagger\rangle\langle\hat{n}_1\rangle)]. \tag{B3}$$

We mention that the same results can be obtained with the help of the Jordan-Schwinger angular momentum operators [52], see, e.g., [11].

2. Single-mode intensity detection

The calculation is similar to the previous one and we obtain in the single-intensity detection scenario,

$$\Delta^2\hat{N}_4 = \sin^4\left(\frac{\varphi}{2}\right)\Delta^2\langle\hat{n}_0\rangle + \cos^4\left(\frac{\varphi}{2}\right)\Delta^2\langle\hat{n}_1\rangle + \frac{\sin^2\varphi}{4}(\langle\hat{n}_0\rangle + \langle\hat{n}_1\rangle + 2\langle\hat{n}_0\rangle\langle\hat{n}_1\rangle - 2|\langle\hat{a}_0\rangle|^2|\langle\hat{a}_1^\dagger\rangle|^2)$$

$$+ \frac{\sin^2\varphi}{2}\mathrm{Re}\big(\langle\hat{a}_0^2\rangle\langle(\hat{a}_1^\dagger)^2\rangle - \langle\hat{a}_0\rangle^2\langle\hat{a}_1^\dagger\rangle^2\big) - \sin\varphi\mathrm{Re}\langle\hat{a}_0\rangle\langle\hat{a}_1^\dagger\rangle - 2\sin^2\left(\frac{\varphi}{2}\right)\sin\varphi\mathrm{Re}[(\langle\hat{a}_0^\dagger\hat{n}_0\rangle - \langle\hat{n}_0\rangle\langle\hat{a}_0^\dagger\rangle)\langle\hat{a}_1\rangle]$$

$$-2\cos^2\left(\frac{\varphi}{2}\right)\sin\varphi\mathrm{Re}(\langle\hat{a}_0^\dagger\rangle(\langle\hat{n}_1\hat{a}_1\rangle - \langle\hat{a}_1\rangle\langle\hat{n}_1\rangle)). \tag{B4}$$

3. Balanced homodyne detection

Using Eq. (10) we immediately have

$$|\partial_\varphi\langle\hat{X}_{\phi_L}\rangle| = \left|\cos\left(\frac{\varphi}{2}\right)\mathrm{Re}(e^{-i\phi_L}\langle\hat{a}_0\rangle) + \sin\left(\frac{\varphi}{2}\right)\mathrm{Re}(e^{-i\phi_L}\langle\hat{a}_1\rangle)\right|. \tag{B5}$$

The variance of the operator $\hat{X}_{\phi_L}$ is found to be

$$\Delta^2\hat{X}_{\phi_L} = \frac{1}{4} + \frac{\sin^2\left(\frac{\varphi}{2}\right)}{2}\big[\mathrm{Re}\big(e^{-i2\phi_L}\big(\langle\hat{a}_0^2\rangle - \langle\hat{a}_0\rangle^2\big)\big) + \langle\hat{n}_0\rangle - |\langle\hat{a}_0\rangle|^2\big]$$

$$+ \frac{\cos^2\left(\frac{\varphi}{2}\right)}{2}\big[\mathrm{Re}\big(e^{-i2\phi_L}\big(\langle\hat{a}_1^2\rangle - \langle\hat{a}_1\rangle^2\big)\big) + \langle\hat{n}_1\rangle - |\langle\hat{a}_1\rangle|^2\big]. \tag{B6}$$

APPENDIX C: THE IMPACT OF NONUNIT PHOTODETECTION EFFICIENCY

If we consider photodetectors having a nonunit quantum efficiency, we model the losses by including a fictitious beam splitter of transmission $\sqrt{\eta}$ in front of an ideal photodetector [36,40,41]. Assuming such a beam splitter in front of the photodetector at the output port k, we have the new annihilation operator

$$\hat{a}'_k = \sqrt{\eta}\hat{a}_k + \sqrt{1-\eta}\hat{a}_v, \tag{C1}$$

where $\hat{a}_v$ is the annihilation operator from the "vacuum port." As a convention, $\eta = 1$ implies an ideal photodetector. We find immediately

$$\langle\hat{n}'_k\rangle = \eta\langle\hat{n}_k\rangle \tag{C2}$$

because the port v is always in the vacuum state. After some computations we also have

$$\Delta^2\hat{n}'_k = \eta^2\Delta^2\hat{n}_k + \eta(1-\eta)\langle\hat{n}_k\rangle. \tag{C3}$$

If we consider the output port 4, we arrive at $\Delta\varphi'_{sg}$ from Eq. (40).

In the case of a difference-intensity detection scenario, Eq. (B3) is modified to

$$\Delta^2\hat{N}'_d = \eta^2\Delta^2\hat{N}_d + \eta(1-\eta)(\langle\hat{n}_4\rangle + \langle\hat{n}_5\rangle), \tag{C4}$$

therefore the phase sensitivity gives

$$\Delta\varphi'_{\mathrm{df}} = \frac{\sqrt{\Delta^2\hat{N}_d + \frac{1-\eta}{\eta}(\langle\hat{n}_4\rangle + \langle\hat{n}_5\rangle)}}{|\partial_\varphi\langle\hat{N}_d\rangle|}. \tag{C5}$$

A similar calculation can be performed to include losses for a balanced homodyne detection and we obtain

$$\Delta\varphi'_{\mathrm{hom}} = \frac{\sqrt{\Delta^2\hat{X}_L + \frac{1}{4}\frac{1-\eta}{\eta}}}{|\partial_\varphi\langle\hat{X}_L\rangle|}. \tag{C6}$$

APPENDIX D: CALCULATIONS FOR A SQUEEZED-COHERENT PLUS SQUEEZED VACUUM INPUT

The input state from Eq. (16) being factorized (separable) allows a separate analysis of the input ports.

For the input port 0 we have a squeezed vacuum state generated by the squeezing operator (17) with the parameter $\xi = re^{i\theta}$. The two basic equations needed in all calculations are [43,44]

$$\hat{S}_0^\dagger(\xi)\hat{a}_0\hat{S}_0(\xi) = \cosh r\hat{a}_0 - \sinh re^{i\theta}\hat{a}_0^\dagger,$$

$$\hat{S}_0^\dagger(\xi)\hat{a}_0^\dagger\hat{S}_0(\xi) = \cosh r\hat{a}_0^\dagger - \sinh re^{-i\theta}\hat{a}_0. \tag{D1}$$

From Eqs. (D1) and considering the input state (16) we have $\langle\hat{a}_0\rangle = 0 = \langle\hat{a}_0^\dagger\rangle$. The average number of photons for a squeezed vacuum state is $\langle\hat{n}_0\rangle = \sinh^2 r$ and its variance

yields

$$\Delta^2 \hat{n}_0 = \frac{\sinh^2 2r}{2}. \tag{D2}$$

At input port 1 we have a squeezed-coherent state, thus using Eqs. (D1) and the properties of coherent states, we have $\langle \hat{a}_1 \rangle = \alpha$, $\langle \hat{a}_1^\dagger \rangle = \alpha^*$. and the average number of photons is found to be $\langle \hat{n}_1 \rangle = |\alpha|^2 + \sinh^2 z$. We find the results

$$\langle \hat{a}_1^2 \rangle = \alpha^2 - \frac{1}{2} \sinh 2z e^{i\phi},$$
$$\langle (\hat{a}_1^\dagger)^2 \rangle = (\alpha^*)^2 - \frac{1}{2} \sinh 2z e^{-i\phi}. \tag{D3}$$

In order to compute the variance we first calculate $\langle \hat{n}_1^2 \rangle = 1/2 \sinh^2 2z + |\alpha|^2 + 2|\alpha|^2 \sinh^2 z$. Using this result and the

average squared $\langle \hat{n}_1 \rangle^2$ we have the variance

$$\Delta^2 \hat{n}_1 = \frac{\sinh^2 2z}{2} + \Upsilon^-(\alpha, \zeta). \tag{D4}$$

1. Fisher information calculations

For a squeezed-coherent plus squeezed vacuum input given by Eq. (16), using Eqs. (A5), (D2), and (D4), we get a sum-sum Fisher matrix coefficient

$$\mathcal{F}_{ss} = \frac{\sinh^2 2r}{2} + \frac{\sinh^2 2z}{2} + \Upsilon^-(\alpha, \zeta). \tag{D5}$$

We also compute $\mathcal{F}_{sd}$ from (A7) and get $\mathcal{F}_{sd} = 0$. Using Eq. (A6) and the previous results we also calculate $\mathcal{F}_{dd}$ given by Eq. (19).

2. Difference intensity detection

We start from Eq. (B3) and replace the terms with the expressions from Eqs. (D2)–(D4). Using the identity $2 \sinh^2 r + 1 = \cosh 2r$ takes us to the final result from Eq. (25). The phase sensitivity $\Delta\varphi_{\mathrm{df}}$ is obtained using Eqs. (24) and (25), yielding

$$\Delta\varphi_{\mathrm{df}} = \frac{\sqrt{\left(\frac{\sinh^2 2r}{2} + \frac{\sinh^2 2z}{2} + \Upsilon^-(\alpha, \zeta)\right)\cot^2 \varphi + \Upsilon^-(\alpha, \xi) + \frac{\cosh 2r \cosh 2z + \sinh 2r \sinh 2z \cos(\phi - \theta)}{2} - \frac{1}{2}}}{\left||\alpha|^2 + \sinh^2 z - \sinh^2 r\right|}. \tag{D6}$$

We impose now the optimum working point $\varphi_{\mathrm{opt}} = \pi/2$ and have the result from Eq. (26).

3. Single-mode intensity detection

Starting from Eq. (B4) and using the previous results takes us to Eq. (29). The phase sensitivity for a single-mode intensity detection scenario is given by

$$\Delta\varphi_{\mathrm{sg}} = \frac{\sqrt{\cot^2\left(\frac{\varphi}{2}\right)\left(\frac{\sinh^2 2z}{2} + \Upsilon^-(\alpha, \zeta)\right) + \tan^2\left(\frac{\varphi}{2}\right)\frac{\sinh^2 2r}{2} + \Upsilon^-(\alpha, \xi) + \frac{\cosh 2r \cosh 2z + \sinh 2r \sinh 2z \cos(\theta - \phi) - 1}{2}}}{\left||\alpha|^2 + \sinh^2 z - \sinh^2 r\right|}. \tag{D7}$$

If we impose now the optimum internal phase shift φ_{opt} from Eq. (30), we obtain the result

$$\Delta\tilde{\varphi}_{\mathrm{sg}} = \frac{\sqrt{\sinh 2r \sqrt{\sinh^2 2z + 2\Upsilon^-(\alpha, \zeta)} + \Upsilon^-(\alpha, \xi) + \frac{\cosh 2r \cosh 2z + \sinh 2r \sinh 2z \cos(\theta - \phi) - 1}{2}}}{\left||\alpha|^2 + \sinh^2 z - \sinh^2 r\right|}. \tag{D8}$$

Further imposing the input phase-matching conditions (20) and (21) yields the best achievable sensitivity

$$\Delta\tilde{\varphi}_{\mathrm{sg}}\big|_{\theta - \phi = \pm\pi} = \frac{\sqrt{\sinh 2r \sqrt{\sinh^2 2z + 2|\alpha|^2 e^{2z}} + |\alpha|^2 e^{-2r} + \sinh^2(r - z)}}{\left||\alpha|^2 + \sinh^2 z - \sinh^2 r\right|}. \tag{D9}$$

Imposing the phase-matching conditions (20) and (37) we obtain

$$\Delta\tilde{\varphi}_{\mathrm{sg}}\big|_{\theta - \phi = 0} = \frac{\sqrt{\sinh 2r \sqrt{\sinh^2 2z + 2|\alpha|^2 e^{-2z}} + |\alpha|^2 e^{-2r} + \sinh^2(r + z)}}{\left||\alpha|^2 + \sinh^2 z - \sinh^2 r\right|}. \tag{D10}$$

The limit value of $|\alpha|$, where phase sensitivity from Eq. (D10) outperforms the one from Eq. (D9) is given by Eq. (39).

APPENDIX E: THE OPTIMIZATION OF TWO INPUT SQUEEZERS

In the most general case we have the input state from Eq. (43), however we focus here on the squeezing part of this state (the discussion thus applies to Sec. III, too). Consider the input state

$$|\psi_{\mathrm{in}}\rangle \approx \hat{S}_1(\zeta)\hat{S}_0(\xi)|0\rangle = e^{[\zeta^* \hat{a}_1^2 - \zeta(\hat{a}_1^\dagger)^2]/2} e^{[\xi^* \hat{a}_0^2 - \xi(\hat{a}_0^\dagger)^2]/2}|0\rangle. \tag{E1}$$

We use the decomposition [53] (we recall $\chi = s e^{i\vartheta}$)

$$e^{[\chi^* \hat{a}_m^2 - \chi(\hat{a}_m^\dagger)^2]/2} = e^{-\tau \chi(\hat{a}_m^\dagger)^2/2} e^{-\nu(\hat{a}_m^\dagger \hat{a}_m + \frac{1}{2})} e^{\tau \hat{a}_m^2/2}, \tag{E2}$$

where $\tau = e^{i\vartheta} \tanh s$ and $\nu = \ln \cosh s$. Now applying Eq. (E2) to our input state allows a sizable simplification since the annihilation operators and the number operators give no contribution when applied to the vacuum state and we have

$$|\psi_{\mathrm{in}}\rangle \approx \frac{1}{\sqrt{\cosh r \cosh z}} e^{-\tau_1(\hat{a}_1^\dagger)^2/2} e^{-\tau_0(\hat{a}_0^\dagger)^2/2}|0\rangle, \tag{E3}$$

where $\tau_1 = e^{i\phi}\tanh z$ and $\tau_0 = e^{i\theta}\tanh r$. Since the input creation operators commute, we can group together the exponentials. We want to find out the state vector $|\psi'\rangle$ after the first beam splitter. Using the field operator transformations (2) we have

$$|\psi'\rangle \approx \frac{1}{\sqrt{\cosh r \cosh z}} e^{\frac{\tau_1 - \tau_0}{2}[(\hat{a}_2^\dagger)^2 - (\hat{a}_3^\dagger)^3] - i(\tau_1 + \tau_0)\hat{a}_2^\dagger \hat{a}_3^\dagger}|0\rangle. \quad (E4)$$

We want to have inside the interferometer as much as possible two single-mode squeezed vacuums [6] (one acting as a phase reference for the other). This condition in reinforced when $\mathrm{Arg}(\tau_1) = \mathrm{Arg}(\tau_0) + \pi$. As remarked by Lang and Caves [6], if we assume $\zeta = -\xi$, i.e., start with the input state $|\psi_{\mathrm{in}}\rangle \approx \hat{S}_1(-\xi)\hat{S}_0(\xi)|0\rangle$, we find after the beam splitter $|\psi'\rangle \approx (\cosh r)^{-1} e^{-\tau_0[(\hat{a}_2^\dagger)^2 - (\hat{a}_3^\dagger)^3]}|0\rangle = \hat{S}_3(-\xi)\hat{S}_2(\xi)|0\rangle$.

The state vector $|\psi'\rangle$ is relevant when computing the QFI, however for realistic schemes we might be interested to find $|\psi_{\mathrm{out}}\rangle$. Starting from the input state (E1) and using the field operator transformations (3) we find

$$|\psi_{\mathrm{out}}\rangle \approx \frac{1}{\sqrt{\cosh r \cosh z}} e^{-\frac{1}{2}\{[\tau_0 \sin^2(\frac{\varphi}{2}) + \tau_1 \cos^2(\frac{\varphi}{2})](\hat{a}_4^\dagger)^2 + [\tau_0 \cos^2(\frac{\varphi}{2}) + \tau_1 \sin^2(\frac{\varphi}{2})](\hat{a}_5^\dagger)^2 + (\tau_1 - \tau_0)\sin\varphi \hat{a}_4^\dagger \hat{a}_5^\dagger\}}|0\rangle. \quad (E5)$$

If we impose now the constraint $\zeta = -\xi$ Eq. (E5) becomes

$$|\psi_{\mathrm{out}}\rangle \approx \frac{1}{\cosh r} e^{-\frac{1}{2}[-\tau_0 \cos\varphi(\hat{a}_4^\dagger)^2 + \tau_0 \cos\varphi(\hat{a}_5^\dagger)^2 - 2\tau_0 \sin\varphi \hat{a}_4^\dagger \hat{a}_5^\dagger]}|0\rangle. \quad (E6)$$

This state has a strong φ dependence, therefore applying the observables described in Sec. II C will yield φ-dependent results. If we now apply at the input two identical squeezings, i.e., $\zeta = \xi$, from Eq. (E5) we get

$$|\psi_{\mathrm{out}}\rangle \approx \frac{1}{\cosh r} e^{-\frac{1}{2}[-\tau_0(\hat{a}_4^\dagger)^2 + \tau_0(\hat{a}_5^\dagger)^2]}|0\rangle \quad (E7)$$

and this is the worst case scenario since this state has no φ dependence whatsoever.

APPENDIX F: CALCULATIONS FOR THE SQUEEZED-COHERENT PLUS SQUEEZED-COHERENT INPUT

In this Appendix we detail the calculations needed for the scenario discussed in Sec. IV. We rely on results already computed in Appendix D. The new results needed to complete the calculations are

$$\langle \hat{n}_1 \hat{a}_1 \rangle - \langle \hat{n}_1 \rangle\langle \hat{a}_1 \rangle = \alpha \sinh^2 z - \frac{\alpha^*}{2}\sinh 2z e^{i\phi},$$

$$\langle \hat{a}_1^\dagger \hat{n}_1 \rangle - \langle \hat{n}_1 \rangle\langle \hat{a}_1^\dagger \rangle = \alpha^* \sinh^2 z - \frac{\alpha}{2}\sinh 2z e^{-i\phi}, \quad (F1)$$

and similarly for port 0,

$$\langle \hat{n}_0 \hat{a}_0 \rangle - \langle \hat{n}_0 \rangle\langle \hat{a}_0 \rangle = \beta \sinh^2 r - \frac{\beta^*}{2}\sinh 2r e^{i\theta},$$

$$\langle \hat{a}_0^\dagger \hat{n}_0 \rangle - \langle \hat{n}_0 \rangle\langle \hat{a}_0^\dagger \rangle = \beta^* \sinh^2 r - \frac{\beta}{2}\sinh 2r e^{-i\theta}. \quad (F2)$$

We also state the result of a term that appears repeatedly,

$$\langle (\hat{a}_0^\dagger)^2 \hat{a}_1^2 \rangle + \langle \hat{a}_0^2(\hat{a}_1^\dagger)^2 \rangle = 2|\alpha\beta|^2 \cos(2\theta_\alpha - 2\theta_\beta)$$
$$- |\beta|^2 \sinh 2z \cos(2\theta_\beta - \phi)$$
$$- |\alpha|^2 \sinh 2r \cos(2\theta_\alpha - \theta)$$
$$+ \frac{1}{2}\sinh 2r \sinh 2z \cos(\theta - \phi). \quad (F3)$$

1. Fisher information calculations

We use the definition of the Fisher matrix element $\mathcal{F}_{ss}$ and the result from Eq. (D4) to obtain

$$\mathcal{F}_{ss} = \frac{\sinh^2 2r}{2} + \Upsilon^-(\beta, \xi) + \frac{\sinh^2 2z}{2} + \Upsilon^-(\alpha, \zeta). \quad (F4)$$

In the calculation of the Fisher information, the most important matrix element is $\mathcal{F}_{dd}$. Applying the input state (43) to the definition from Eq. (A3) gives the result

$$\mathcal{F}_{dd} = \Upsilon^+(\beta, \zeta) + \Upsilon^+(\alpha, \xi)$$
$$+ \frac{\cosh 2r \cosh 2z - \sinh 2r \sinh 2z \cos(\theta - \phi) - 1}{2}. \quad (F5)$$

Finally, the last Fisher matrix element yields

$$\mathcal{F}_{sd} = |\alpha\beta|[\sinh 2r \sin(\theta_\alpha + \theta_\beta - \theta)$$
$$- \sinh 2z \sin(\theta_\alpha + \theta_\beta - \phi)$$
$$- 2(1 + \sinh^2 r + \sinh^2 z)\sin(\theta_\alpha - \theta_\beta)]. \quad (F6)$$

2. Phase-matching conditions for optimum Fisher information

As stated in Sec. IV A, we start from a known scenario and make our way towards this more general case. If $|\beta| \to 0$, we find ourselves in the squeezed-coherent plus squeezed vacuum input scenario from Sec. III. The phase-matching conditions have been discussed and yield the Fisher information from Eq. (22). Therefore, we now apply the constraints from Eqs. (20) and (21) on the Fisher matrix elements $\mathcal{F}_{ss}$, $\mathcal{F}_{dd}$, and $\mathcal{F}_{sd}$ from Eqs. (F4), (F5), and (F6), respectively. The Fisher information definition from Eq. (12) takes us to

$$\mathcal{F} = \Upsilon^+(\beta, \zeta) + |\alpha|^2 e^{2r} + \sinh^2(r + z)$$
$$- \frac{|\alpha\beta|^2 \sin^2(\theta_\alpha - \theta_\beta)(e^{2r} + e^{2z})^2}{\frac{\sinh^2 2r}{2} + \Upsilon^-(\beta, \xi) + \frac{\sinh^2 2z}{2} + |\alpha|^2 e^{2z}}. \quad (F7)$$

We allowed $\beta \neq 0$, and since $\beta = |\beta|e^{i\theta_\beta}$ we have to define the angle of the second coherent input θ_β. It can be easily shown that the Fisher information from Eq. (F7) is maximized only for $\theta_\alpha - \theta_\beta = n\pi/2$ with $n \in \mathbb{Z}$. In Ref. [7] it has been shown that for a double coherent input, the maximum Fisher

information is achieved when

$$\theta_\alpha - \theta_\beta = 0. \tag{F8}$$

We thus adopt the PMCs given by Eq. (44), impose this constraint on Eq. (F7), and have immediately the QFI from Eq. (45). This Fisher information is clearly optimal as $|\beta| \to 0$, however, there is no reason to be so when $|\beta|$ is comparable with the other parameters. The poor performance comes from the first term of Eq. (F7), namely $\Upsilon^+(\beta, \zeta)$. Indeed, in Eq. (45) it takes its minimal value due to the implied phase-matching condition $2\theta_\beta - \phi = \pm\pi$. In order to maximize the term $\Upsilon^+(\beta, \zeta)$ from Eqs. (F7) or (F5) we need to impose the phase-matching condition

$$2\theta_\beta - \phi = 0. \tag{F9}$$

However, it is easy to see that this PMC cannot be satisfied simultaneously with Eqs. (20), (21), and (F8). We have two solutions to this problem:

(i) Continue to impose the PMC from Eq. (F8) and accept that $\Upsilon^+(\beta, \zeta) = |\beta|^2 e^{-2z}$.

(ii) Impose $\theta_\alpha - \theta_\beta = \pm\pi/2$ and a whole new discussion begins.

Thus, in case (i) we end up with a trade-off situation and we have to choose which two among three terms from Eq. (F5) are to be maximized. If the coherent sources are dominant over the contribution from squeezing, it is natural to maximize $\Upsilon^+(\beta, \zeta)$ and $\Upsilon^+(\alpha, \xi)$. This leads to the PMCs given by Eq. (46) and to the QFI given by Eq. (47).

Up to this point we assumed that the constraint (F8) yields the maximum Fisher information, and this is certainly true in the high-coherent regime $\{|\alpha|, |\beta|\} \gg \{\sinh r, \sinh z\}$. However, in the $\{|\alpha|, |\beta|\} \ll \{\sinh r, \sinh z\}$ regime this is not necessarily true. We thus consider the case (ii) now, namely when $\theta_\alpha - \theta_\beta = (2k+1)\pi/2$ with $k \in \mathbb{Z}$. Returning again to the Fisher matrix element $\mathcal{F}_{dd}$ from Eq. (F5) we note that there is actually a PMC allowing us to simultaneously maximize all terms, namely Eq. (49). The penalty for this constraint is the fact that $\mathcal{F}_{sd} \neq 0$ and we have the QFI given by Eq. (50).

3. Difference-intensity detection

For the input state given by Eq. (43) the variance of $\hat{N}_d$ is found to be

$$\Delta^2 \hat{N}_d = \cos^2\varphi \left(\frac{\sinh^2 2r}{2} + \Upsilon^-(\beta, \xi) + \frac{\sinh^2 2z}{2} + \Upsilon^-(\alpha, \zeta) \right)$$

$$+ \sin^2\varphi \left(\Upsilon^-(\beta, \zeta) + \Upsilon^-(\alpha, \xi) + \frac{\cosh 2r \cosh 2z + \sinh 2r \sinh 2z \cos(\theta - \phi)}{2} - \frac{1}{2} \right)$$

$$+ \sin 2\varphi |\beta\alpha| [2(\sinh^2 r - \sinh^2 z)\cos(\theta_\alpha - \theta_\beta) - \sinh 2r \cos(\theta_\alpha + \theta_\beta - \theta) + \sinh 2z \cos(\theta_\alpha + \theta_\beta - \phi)]. \tag{F10}$$

Using the result from Eq. (56) and the one above, allows the phase sensitivity to be written as

$$\Delta\varphi_{\text{df}} = \frac{\sqrt{\Delta^2 \hat{N}_d}}{|\sin\varphi(|\alpha|^2 - |\beta|^2 + \sinh^2 z - \sinh^2 r) + 2\cos\varphi|\alpha\beta|\cos(\theta_\alpha - \theta_\beta)|}. \tag{F11}$$

Similar to the previous scenarios an optimum total internal phase shift φ_{opt} can be found. We make the following notations:

$$A = \frac{\sinh^2 2r}{2} + \Upsilon^-(\beta, \xi) + \frac{\sinh^2 2z}{2} + \Upsilon^-(\alpha, \zeta),$$

$$B = \Upsilon^-(\beta, \zeta) + \Upsilon^-(\alpha, \xi) + \frac{\cosh 2r \cosh 2z + \sinh 2r \sinh 2z \cos(\theta - \phi)}{2} - \frac{1}{2},$$

$$C = |\alpha\beta|[2(\sinh^2 r - \sinh^2 z)\cos(\theta_\alpha - \theta_\beta) - \sinh 2r \cos(\theta_\alpha + \theta_\beta - \theta) + \sinh 2z \cos(\theta_\alpha + \theta_\beta - \phi)],$$

$$D = |\alpha|^2 - |\beta|^2 + \sinh^2 z - \sinh^2 r, \quad F = 2|\alpha\beta|\cos(\theta_\alpha - \theta_\beta). \tag{F12}$$

With these notations, a simple calculation shows that the optimum phase shift is given by

$$\varphi_{\text{opt}} = \arctan\left(\frac{AD - CF}{BF - CD} \right) + k\pi, \tag{F13}$$

with $k \in \mathbb{Z}$. Inserting φ_{opt} into Eq. (F11) yields the optimum phase sensitivity $\Delta\tilde{\varphi}_{\text{df}}$.

4. Single-mode intensity detection

From Eq. (B4), using the input state given by Eq. (43) and the results mentioned earlier, we have

$$\Delta^2 \hat{N}_4 = \sin^4\left(\frac{\varphi}{2}\right)\left(\frac{\sinh^2 2r}{2} + \Upsilon^-(\beta, \xi) \right) + \cos^4\left(\frac{\varphi}{2}\right)\left(\frac{\sinh^2 2z}{2} + \Upsilon^-(\alpha, \zeta) \right)$$

$$+ \frac{\sin^2\varphi}{4}\left(\Upsilon^-(\beta, \zeta) + \Upsilon^-(\alpha, \xi) + \frac{\cosh 2r \cosh 2z + \sinh 2r \sinh 2z \cos(\theta - \phi)}{2} - \frac{1}{2} \right)$$

$$-\sin\varphi|\beta\alpha|\Big(\cos(\theta_\alpha-\theta_\beta)+\sin^2\Big(\frac{\varphi}{2}\Big)[2\sinh^2 r\cos(\theta_\alpha-\theta_\beta)-\sinh 2r\cos(\theta_\alpha+\theta_\beta-\theta)]$$

$$+\cos^2\Big(\frac{\varphi}{2}\Big)[2\sinh^2 z\cos(\theta_\alpha-\theta_\beta)-\sinh 2z\cos(\theta_\alpha+\theta_\beta-\phi)]\Big). \tag{F14}$$

Using the previous result and Eq. (58), we find the phase sensitivity for a single-mode intensity detection,

$$\Delta\varphi_{\text{sg}}=\frac{\sqrt{\Delta^2\hat{N}_4}}{\left|\frac{1}{2}(|\alpha|^2-|\beta|^2+\sinh^2 z-\sinh^2 r)+|\alpha\beta|\cos(\theta_\alpha-\theta_\beta)\right|}. \tag{F15}$$

[1] J. Aasi *et al.* (The LIGO Scientific Collaboration), Nat. Photon. **7**, 613 (2013).

[2] M. A. Taylor, J. Janousek, V. Daria, J. Knittel, B. Hage, H.-A. Bachor, and W. P. Bowen, Nat. Photon. **7**, 229 (2013).

[3] B. T. Gard, C. You, D. K. Mishra, R. Singh, H. Lee, T. R. Corbitt, and J. P. Dowling, EPJ Quantum Technol. **4**, 4 (2017).

[4] D. Li, C.-H. Yuan, Z. Y. Ou, and W. Zhang, New J. Phys. **16**, 073020 (2014).

[5] M. D. Lang and C. M. Caves, Phys. Rev. Lett. **111**, 173601 (2013).

[6] M. D. Lang and C. M. Caves, Phys. Rev. A **90**, 025802 (2014).

[7] S. Ataman, A. Preda, and R. Ionicioiu, Phys. Rev. A **98**, 043856 (2018).

[8] M. Takeoka, K. P. Seshadreesan, C. You, S. Izumi, and J. P. Dowling, Phys. Rev. A **96**, 052118 (2017).

[9] A. Preda and S. Ataman, Phys. Rev. A **99**, 053810 (2019).

[10] V. Michaud-Belleau, J. Genest, and J.-D. Deschênes, Phys. Rev. Appl. **10**, 024025 (2018).

[11] R. Demkowicz-Dobrzański, M. Jarzyna, and J. Kołodyński, Prog. Opt. **60**, 345 (2015).

[12] F. Acernese, M. Agathos, K. Agatsuma, D. Aisa, N. Allemandou *et al.*, Class. Quantum Grav. **32**, 024001 (2014).

[13] E. Oelker, L. Barsotti, S. Dwyer, D. Sigg, and N. Mavalvala, Opt. Express **22**, 21106 (2014).

[14] M. Mehmet and H. Vahlbruch, Class. Quantum Grav. **36**, 015014 (2018).

[15] H. Vahlbruch, D. Wilken, M. Mehmet, and B. Willke, Phys. Rev. Lett. **121**, 173601 (2018).

[16] V. Giovannetti and L. Maccone, Phys. Rev. Lett. **108**, 210404 (2012).

[17] C. M. Caves, Phys. Rev. D **23**, 1693 (1981).

[18] M. Xiao, L.-A. Wu, and H. J. Kimble, Phys. Rev. Lett. **59**, 278 (1987).

[19] V. Giovannetti, S. Lloyd, and L. Maccone, Science **306**, 1330 (2004).

[20] L. Pezzé and A. Smerzi, Phys. Rev. Lett. **100**, 073601 (2008).

[21] M. Jarzyna and R. Demkowicz-Dobrzański, Phys. Rev. A **85**, 011801(R) (2012).

[22] J.-Y. Wu, N. Toda, and H. F. Hofmann, Phys. Rev. A **100**, 013814 (2019).

[23] S. C. Burd, R. Srinivas, J. J. Bollinger, A. C. Wilson, D. J. Wineland, D. Leibfried, D. H. Slichter, and D. T. C. Allcock, Science **364**, 1163 (2019).

[24] M. Malnou, D. A. Palken, B. M. Brubaker, L. R. Vale, G. C. Hilton, and K. W. Lehnert, Phys. Rev. X **9**, 021023 (2019).

[25] C. Xu, L. Zhang, S. Huang, T. Ma, F. Liu, H. Yonezawa, Y. Zhang, and M. Xiao, Photon. Res. **7**, A14 (2019).

[26] H. Grote, K. Danzmann, K. L. Dooley, R. Schnabel, J. Slutsky, and H. Vahlbruch, Phys. Rev. Lett. **110**, 181101 (2013).

[27] H. Vahlbruch, M. Mehmet, K. Danzmann, and R. Schnabel, Phys. Rev. Lett. **117**, 110801 (2016).

[28] R. Schnabel, Phys. Rep. **684**, 1 (2017).

[29] B. Yurke, S. L. McCall, and J. R. Klauder, Phys. Rev. A **33**, 4033 (1986).

[30] L. Pezzé, A. Smerzi, G. Khoury, J. F. Hodelin, and D. Bouwmeester, Phys. Rev. Lett. **99**, 223602 (2007).

[31] M. G. Paris, Phys. Lett. A **201**, 132 (1995).

[32] S. L. Braunstein and C. M. Caves, Phys. Rev. Lett. **72**, 3439 (1994).

[33] R. Demkowicz-Dobrzański, J. Kołodyński, and M. Guţă, Nat. Commun. **3**, 1063 (2012).

[34] L. Pezzè, P. Hyllus, and A. Smerzi, Phys. Rev. A **91**, 032103 (2015).

[35] C. Sparaciari, S. Olivares, and M. G. A. Paris, J. Opt. Soc. Am. B **32**, 1354 (2015).

[36] C. Sparaciari, S. Olivares, and M. G. A. Paris, Phys. Rev. A **93**, 023810 (2016).

[37] J. Liu, X. Jing, and X. Wang, Phys. Rev. A **88**, 042316 (2013).

[38] U. Dorner, R. Demkowicz-Dobrzanski, B. J. Smith, J. S. Lundeen, W. Wasilewski, K. Banaszek, and I. A. Walmsley, Phys. Rev. Lett. **102**, 040403 (2009).

[39] R. Demkowicz-Dobrzanski, U. Dorner, B. J. Smith, J. S. Lundeen, W. Wasilewski, K. Banaszek, and I. A. Walmsley, Phys. Rev. A **80**, 013825 (2009).

[40] T. Ono and H. F. Hofmann, Phys. Rev. A **81**, 033819 (2010).

[41] T. Kim, Y. Ha, J. Shin, H. Kim, G. Park, K. Kim, T.-G. Noh, and C. K. Hong, Phys. Rev. A **60**, 708 (1999).

[42] M. G. A. Paris, Int. J. Quantum Info. **07**, 125 (2009).

[43] C. Gerry and P. Knight, *Introductory Quantum Optics* (Cambridge University Press, Cambridge, 2005).

[44] L. Rodney, *The Quantum Theory of Light (Third Edition)* (Oxford University Press, Oxford, 2000).

[45] H. P. Yuen, Phys. Rev. A **13**, 2226 (1976).

[46] L. Mandel and E. Wolf, *Optical Coherence and Quantum Optics* (Cambridge University Press, Cambridge, 1995).

[47] G. S. Agarwal, *Quantum Optics* (Cambridge University Press, Cambridge, 2012).

[48] M. S. Kim and B. C. Sanders, Phys. Rev. A **53**, 3694 (1996).

[49] Z. Y. Ou, Phys. Rev. Lett. **77**, 2352 (1996).

[50] H. F. Hofmann, Phys. Rev. A **79**, 033822 (2009).

[51] O. Pinel, J. Fade, D. Braun, P. Jian, N. Treps, and C. Fabre, Phys. Rev. A **85**, 010101(R) (2012).

[52] J. Schwinger, On angular momentum, in *Quantum Theory of Angular Momentum*, edited by L. Biedenharn and H. V. Dam (Academic, New York, 1965).

[53] D. R. Truax, Phys. Rev. D **31**, 1988 (1985).